



INAOE

**INSTITUTO NACIONAL DE ASTROFÍSICA
ÓPTICA Y ELECTRÓNICA**

DEPARTAMENTO DE ELECTRÓNICA

*“Synthesis, characterization and application of
porous silicon decorated with TiO₂ in electronic
devices and sensors”*

TESIS PRESENTADA PARA OBTENER EL TÍTULO DE:

**DOCTOR EN CIENCIAS EN LA ESPECIALIDAD DE
ELECTRÓNICA**

PRESENTA:
ABEL GARZÓN ROMÁN

ASESORES:

DR. CARLOS ZÚNIGA ISLAS, INAOE

DR. ENRIQUE QUIROGA GONZÁLEZ, BUAP

ABRIL 2022
Tonanzintla, Puebla

©INAOE 2022

Derechos Reservados

El autor otorga al INAOE el permiso de reproducir y distribuir copias de esta tesis en su totalidad o en partes mencionando la fuente.



Agradecimientos

A mis padres Rocío y Abel por brindarme siempre el apoyo, sin importar las decisiones que he tomado. Y este trabajo se lo dedico a mi papá que se fue antes de tiempo y no me vio graduarme, pero que los pequeños triunfos que he logrado y que lograré serán para él donde quiera que este y por supuesto que para mi mamá que aún está conmigo un pilar importante de mi vida.

A mis hermanos Anabel, Griselda, Javier y Daniel por apoyarme y hacerme reconocer los errores que cometo.

A mi sobrino Abraham alias “mi amigo” que hemos estado juntos siempre y doy gracias poder estar con él.

A Bety que me apoyo en momentos críticos cuando lo necesitaba y a pesar de tomar diferentes caminos, se lo sigo agradeciendo de corazón.

A mis directores de tesis Carlos y Enrique, que me apoyaron a lo largo de este proyecto y a los sinodales por haber aceptado participar en la evaluación de este proyecto, María Eugenia, Mario, Alfonso, Alfredo y Valentín.

Al CONACYT, por haberme apoyado con una beca (Número de apoyo 402036)

Al Instituto Nacional de Astrofísica, Óptica y Electrónica (INAOE) y al Instituto de Física de la BUAP (IFUAP) por el apoyo brindado, dando acceso a su infraestructura y a sus técnicos que me apoyaron en algunas caracterizaciones.

RESUMEN

En este trabajo se fabricaron heteroestructuras de dióxido de titanio con silicio poroso. El silicio poroso se preparó por grabado químico asistido por metal (MACE por sus siglas en inglés), para el depósito del dióxido de titanio se usó un método simple llamado síntesis solvotérmica. Fue posible modular la morfología y las características eléctricas del dióxido de titanio, variando la concentración del precursor, el tipo de solvente y agregando metales como dopantes. La morfología de las partículas de TiO_2 depositadas en las paredes del silicio poroso puede ser modulada de partículas alargadas a nanohojuelas variando la concentración del precursor. Por otra parte, usando metanol, etilenglicol y acetona se obtuvieron formas como hojuelas, semiesferas y erizos de mar respectivamente, y las nanoestructuras cambiaron de coliflores a nanocubos al introducir Cu o In como dopantes. El tamaño de las partículas también varía con la concentración del precursor; el tamaño es menor para bajas concentraciones, lo que hace que la energía de banda prohibida y la energía de emisión luminiscente se incrementen. Espectroscopía Raman y difracción de rayos X revelaron la fase cristalina del TiO_2 , lo que corresponde a una fase rutilo o anatasa. Los espectros de fotoluminiscencia mostraron bandas luminiscentes alrededor de 2.9 eV, lo que corresponde a vacancias de oxígeno. Además, un corrimiento a energías más grandes fue observado en estos espectros y dependió de las condiciones de síntesis. Reflectancia difusa y su correspondiente análisis por Kubelka-Munk permitieron determinar la banda prohibida de las estructuras de TiO_2 con y sin dopantes. Una reducción en la banda prohibida fue observada debido a los dopantes. Curvas de corriente contra voltaje mostraron un comportamiento rectificador para voltajes negativos; sin embargo, un efecto de resistencia diferencial negativa, similar al comportamiento de un diodo túnel, fue observado en voltajes positivos para todas las muestras. Además, oscilaciones periódicas fueron observadas en las muestras, siendo la primera vez que se observan en compositos o dispositivos que contienen Si y TiO_2 . Las heteroestructuras de este trabajo representan el oscilador de relajación más simple nunca antes reportado, así como es el primer oscilador de relajación de su tipo. También, las curvas de corriente contra voltaje se midieron en condiciones de oscuridad e iluminación, lo que reveló un efecto de fotocorriente que puede ser usado como fotodetector.

ABSTRACT

In this work, heterostructures of titanium dioxide with porous silicon were fabricated. The porous silicon was prepared by Metal-Assisted Chemical Etching (MACE), and TiO₂ was deposited using a straightforward method called solvothermal synthesis. It was possible to modulate the morphology and optical characteristics of TiO₂ by varying the concentration of the precursor, the kind of solvent, and adding up metal dopants. The morphology of the TiO₂ particles deposited on the walls of porous Si could be modulated from elongated particles to nanoflakes by varying the precursor concentration. On the other hand, their morphology is flake-like, semi-spherical, and sea urchin-like, for methanol, ethylene glycol, and acetone respectively, and it could change from cauliflower-like and nanocubes when going from Cu to In as dopants. The particle size also varies with the precursor concentration; the size is smaller for lower concentrations, producing that the bandgap and emission energy increase. Raman spectroscopy and x-ray diffraction patterns revealed the crystalline phase structure of TiO₂, which corresponds to anatase or rutile. The photoluminescence spectra showed broadbands around 2.9 eV, which can be related to oxygen vacancies. Additionally, a blue shift was observed in the photoluminescence spectra depending on the synthesis conditions. Diffuse reflectance and their corresponding analysis by Kubelka-Munk were used to determine the optical bandgap of the TiO₂ structures with and without dopant. A reduction of the bandgap was observed due to the dopant changes. Current-voltage curves showed a rectifying behavior for negative voltages, while a negative differential resistance effect was observed for positive voltages similar to a tunnel diode behavior in all the samples. Moreover, periodic oscillations were observed in the samples, being the first time that such effect is observed in any TiO₂-Si composites or devices. The heterostructures of this work represent the simplest relaxation oscillator ever reported, and this is also the first relaxation oscillator of its kind. Additionally, current-voltage curves were recorded in darkness and under illumination conditions, which revealed a photocurrent effect that can be used in photodetectors.

CONTENT

<i>CHAPTER 1</i> INTRODUCTION.....	1
1.1 Objectives	5
1.2 Justification.....	5
References.....	6
<i>CHAPTER 2</i> METHODOLOGY.....	11
<i>CHAPTER 3</i> RESULTS AND DISCCUSION.....	17
3.1 Morphological characterization.....	17
3.2 Structural and compositional characterization	26
3.3 Optical characterization	34
3.4 Application as oscillator.....	46
3.5 Application as photosensor	70
References.....	75
<i>CHAPTER 4</i> CONCLUSION.....	84
Products of this work.....	86

CHAPTER 1

INTRODUCTION

Titanium dioxide (TiO_2) is one of the most important semiconductor materials. This material can be found in three crystalline phases called anatase, rutile, and brookite, with a tetragonal structure for the two first phases, while the last phase possesses an orthorhombic structure [1, 2]. Every phase can be obtained at different temperatures [3]. TiO_2 has received enormous attention in the last few years, and it has been widely investigated due to its photoelectric properties, non-toxicity, biocompatibility, thermal stability, chemical resistance [2], and its potential application in photocatalysis [4–7], photovoltaics [8], sensors, batteries, fuel cells, and energy storage [3]. Moreover, TiO_2 has a high dielectric constant ($k \sim 80$) [9]. This material is also transparent to visible light, showing a very high optical transmittance [10]. These characteristics have been very useful in different microelectronic and nanoelectronic applications, such as dielectric in storage capacitors in DRAM and nonvolatile memories [11]. Furthermore, nano-fabrication of this material has demonstrated different properties that have been attributed to quantum effects [10].

There are many ways to synthesize TiO_2 structures, such as sol-gel [3], electrochemical anodization [3], sputtering [12], thermal evaporation [13], solvothermal synthesis [14], direct thermal oxidation [15], hydrothermal synthesis [16], and others [17, 18]. Particularly, the solvothermal method has shown to be a facile and effective method to prepare TiO_2 structures in only one step, allowing to obtain different morphologies, just varying parameters such as temperature, time, additives, solution pH, and solvent medium [19].

The titanium dioxide is the main catalyst in industry and research. Photocatalytic applications have been studied for a long time; however, the efficiency of these systems is very sensitive to defects, which decrease it by contributing to the recombination of photo-generated electron-hole pairs [4]. This (fast) recombination cause problems not only in catalysis applications but also in optoelectronics applications.

Nevertheless, one-dimensional and multi-dimensional hierarchical structures have demonstrated an improvement in the separation of electron/hole pairs, charge carrier transfer, and enlargement of the active surface area compared to that of TiO₂ nanoparticles. This improvement has solved some problems that appear in different applications, mainly in photocatalytic activity [20].

On the other hand, the literature has also reported that TiO₂ doped with transition metals can be a promising strategy to improve the dielectric, ferromagnetic and photocatalytic properties, and to increase its sensitivity in the visible region [21, 22–26].

Also, TiO₂, which usually behaves as an n-type semiconductor, can be obtained as a p-type material due by partially substituting Ti by In Ref. [27]. On the other hand, the use of Cu as a dopant is also crucial because it has high electronic conductivity and can effectively reduce the wide bandgap of TiO₂ through the creation of defects and d-band states. This metallic element can also act as an active trap center for electrons and holes to reduce the rate of electron-hole recombination [28]. Moreover, Cu-doped TiO₂ has exhibited better efficiencies compared to the Au and Ag-doped material [29].

On the other hand, researchers have studied the inclusion of TiO₂ into semiconductor substrates to improve the photocatalytic activity [4]. This inclusion of TiO₂ into a semiconductor is called “Semiconductor coupling”, which employs the immobilization of TiO₂ nanostructures in the semiconductor and this is considered as one of the best ways to

increase the photocatalytic efficiency and the electric response without modifying the optical, electrical, and crystal structure of TiO₂ [4]. Catalyst supports such as carbon, carbon nanotubes, activated carbon, and porous silicon (PS) have been used [5]. Among them, one of the most promising and underexplored supports is porous silicon (PS). The immobilization of metallic oxide nanoparticles inside PS could lead to the creation of a promising technology in photocatalysis [6] and electronics, because its porosity allows the interaction with atoms, ions, and molecules in applications that involve ion exchange, adsorption, and catalysis [7], and its additional (well known in electronics) semiconducting properties.

Even though Uhlir discovered porous silicon (PS) in 1956 [30], it was until 1990 when this material gained attention due to its photoluminescence (PL) properties in the visible range [31]. Up to now, the study of PS is crucial for applications in optoelectronics, microelectronics, sensors, and medical applications [32, 33]. There are many methods to obtain PS layers, but the most important is electrochemical anodization [31], by which PS layers can be obtained in a simple and controlled way. However, the Metal-Assisted Chemical Etching (MACE) method [34] has gained attention in recent years due to its simplicity and low cost in comparison to the electrochemical anodization, which needs the use of a current source.

Combining metallic oxides and PS results in an enhancement of the surface area and enhancement other characteristics. Moreover, it modifies the electrical and optical properties of PS [35]. There are some reports about the immobilization of TiO₂ nanostructures in PS [4–7]. However, the insertion of TiO₂ nanoparticles is commonly performed using high-cost methods such as atomic layer deposition (ALD) [4], or magnetron sputtering [36], to achieve

uniform coatings inside PS. In comparison with those methods, the solvothermal method is a low-cost method. It is only necessary to optimize its many synthesis parameters to be able to obtain the desired crystal structures and morphologies. The supposed low effectiveness of this method is compensated by its simplicity and low cost, in comparison with ALD or sputtering. Additionally, different material morphologies can be obtained by this technique, which is not typical for any other method.

In the literature, heterostructures of TiO₂ with Si have been used to develop devices that are compatible with the microelectronic industry (mainly based on Si). Such heterostructures present p-n junctions, which are essential to separate charges, e.g. for photocatalysis [37], solar cells [38], or photodetectors [39], to mention some applications. However, looking for new effects, PS has been substituting bulk Si in many devices. This material can be used as support [40], with porosities ranging from micro (pore diameters below 2 nm) to macroporosity (pore diameters larger than 50 nm), which can be modulated in-depth [41]. The porosity represents a higher surface area than bulk Si, allowing the faster mass transfer [7]. Additionally, due to the pore walls' defect-rich surface, it has open bonds that can be easily functionalized and could act as nucleation centers to grow other materials and to form composites. Furthermore, this material exhibits optical and electronic bandgaps that can be tuned with the degree of porosity and/ or level of defects [40 and 41]. Taking advantage of these properties, heterostructures composed of TiO₂ and PS have been fabricated, presenting novel or enhanced properties like enhanced photocatalytic activity [4, 42], enhanced fluorescence for sensing [43], enhanced adsorption of gases [44], enhanced light absorption [45], thermoelectric properties [46], etc. However, in most of the cases, the authors did not take full advantage of the pore wall surface properties, since just in a few works, the deposition of TiO₂ went inside the pores (mostly using ALD) [4, 43].

Objective

To investigate the properties of heterostructures of porous silicon decorated with titanium dioxide obtained by the solvothermal synthesis to develop electronic and sensing devices.

Specific objectives

1. To study and characterize the properties of the porous silicon obtained from the MACE method
2. To study and characterize the properties of the titanium dioxide obtained from solvothermal method
3. To study different methodologies to obtain different morphologies of titanium dioxide
4. To develop heterostructures of porous silicon and titanium dioxide
5. To use these heterostructures to develop electronic and sensing devices

Justification:

Titanium dioxide and porous silicon have been studied separated and forming heterostructures; however, most of the investigations focus on catalysis. On the other hand, in most of the cases, the authors did not take full advantage of the pore wall surface properties of porous silicon, since just in a few works the deposition of TiO₂ went inside the pores (mostly using ALD). The present work focuses on the development of heterostructures of porous silicon decorated by TiO₂ by solvothermal synthesis, a simple and economical method, which takes advantage of the surface defects of the pore walls to nucleate TiO₂ nanocrystals. It is envisioned to observe new optical and electrical characteristics to develop electronic and sensing devices.

References

- [1] S.M. Mokhtar, M.K. Ahmad, C.F. Soon, N. Nafarizal, A.B. Faridah, A.B. Suriani, M.H. Mamat, M. Shimomura, K. Murakami, Fabrication and characterization of rutile-phased titanium dioxide (TiO₂) nanorods array with various reaction times using one-step hydrothermal method, *Optik* 154, 510 (2018). <https://doi.org/10.1016/j.ijleo.2017.10.091>
- [2] I.B. Troitskaia, T.A. Gavrilova, V.V. Atuchin, Structure and micromorphology of titanium dioxide nanoporous microspheres formed in water solution *Phys. Procedia* 23, 65 (2012). <https://doi.org/10.1016/j.phpro.2012.01.017>
- [3] M. Abdullaha, S.K. Kamarudina, Titanium dioxide nanotubes (TNT) in energy and environmental applications: An overview, *Renew. Sustain. Energy Rev.* 76, 212 (2017). <https://doi.org/10.1016/j.rser.2017.01.057>
- [4] S. Sampath, P. Maydannik, T. Ivanova, M. Shestakova, T. Homola, A. Bryukvin, V. Alagan, Efficient solar photocatalytic activity of TiO₂ coated nano-porous silicon by atomic layer deposition, *Superlattice Microstruct.* 97, 155 (2016). <https://doi.org/10.1016/j.spmi.2016.06.004>
- [5] C.M. Tank, Y.S. Sakhare, N.S. Kanhe, A.B. Nawale, A.K. Das, S.V. Bhoraskar, V.L. Mathe, Electric field enhanced photocatalytic properties of TiO₂ nanoparticles immobilized in porous silicon template *Solid State Sci.* 13, 1500 (2011). [10.1016/j.solidstatesciences.2011.05.010](https://doi.org/10.1016/j.solidstatesciences.2011.05.010)
- [6] J. Castañeda-Contreras, V.F. Marañón-Ruiz, R. Chiu-Zárate, H. Pérez-Ladrón de Guevara, R. Rodriguez, C. Michel-Urbe, Photocatalytic activity of erbium-doped TiO₂ nanoparticles immobilized in macro-porous silica films *Mater. Res. Bull.* 47, 290 (2012). <https://doi.org/10.1016/j.materresbull.2011.11.021>
- [7] Y.S. Sakhare, S.V. Bhoraskar, V.L. Mathe, A.U. Ubale, Electric field assisted enhanced photo catalytic activities of immobilized nano TiO₂ on porous silicon, *Mater. Res. Bull.* 59, 205 (2014). <https://doi.org/10.1016/j.materresbull.2014.07.006>
- [8] J. Xiong, B. Yang, J. Yuan, L. Fan, X. Hu, H. Xie, L. Lyu, R. Cui, Y. Zou, C. Zhou, D. Niu, Y. Gao, J. Yang, Efficient organic photovoltaics using solution-processed, annealing-free TiO₂ nanocrystalline particles as an interface modification layer *Org. Electron.* 17, 253 (2015). <https://doi.org/10.1016/j.orgel.2014.12.023>

- [9] A. Welte, C. Waldauf, C. Brabec, P.J. Wellmann, Application of optical absorbance for the investigation of electronic and structural properties of sol-gel processed TiO₂ films, *Thin Solid Films* 516, 7256 (2008). <https://doi.org/10.1016/j.tsf.2007.12.025>
- [10] I. Iatsunskyi, M. Jancelewicz, G. Nowaczyk, M. Kempinski, B. Peplinska, M. Jarek, K. Załęski, S. Jurga, V. Smyntyna, Atomic layer deposition TiO₂ coated porous silicon surface: structural characterization and morphological features, *Thin Solid Films* 589, 303 (2015). <https://doi.org/10.1016/j.tsf.2015.05.056>
- [11] M. Ishfaq, M.R. Khan, A. Ali, S. Bhardwaj, C. Cepek, A.S. Bhatti, Optical and electrical characteristics of 17 keV X-rays exposed TiO₂ films and Ag/TiO₂/p-Si MOS device, *Mater. Sci. Semicond. Process.* 63, 107 (2017). <https://doi.org/10.1016/j.mssp.2017.02.009>
- [12] D. Rafieian, W. Ogieglo, T. Savenije, R.G.H. Lammertink, Controlled formation of anatase and rutile TiO₂ thin films by reactive magnetron sputtering *AIP Adv.* 5, 97168 (2015). <https://doi.org/10.1063/1.4931925>
- [13] C.W. Lai, S. Sreekantan, WO₃ Deposited TiO₂ Nanotube Arrays by Thermal Evaporation Method for Effective Photocatalytic Activity *J. Eng. Sci.* 8, 39 (2012).
- [14] X.M. Yan, J. Kang, L. Gao, L. Xiong, P. Mei, Solvothermal synthesis of carbon-coated N-doped TiO₂ nanostructures with enhanced visible light catalytic activity, *Appl. Surf. Sci.* 15, 778 (2013). <https://doi.org/10.1016/j.apsusc.2012.11.111>
- [15] J.M. Wu, T.W. Zhang, Y.W. Zeng, S. Hayakawa, K. Tsuru, A. Osaka, Large-scale preparation of ordered titania nanorods with enhanced photocatalytic activity, *Langmuir* 21, 6995 (2005). <https://doi.org/10.1021/la0500272>
- [16] Z.Y. Yuan, B.L. Su, Titanium oxide nanotubes, nanofibers and nanowires, *Colloids Surf. A* 241, 173 (2004). <https://doi.org/10.1016/j.colsurfa.2004.04.030>
- [17] M. Malekshahi Byranvand, A. Nemati Kharat, L. Fatholahi, Z. Malekshahi Beiranvand, A Review on Synthesis of Nano-TiO₂ via Different Methods *J. Nanostruct.* 3, 1 (2013). 10.7508/JNS.2013.01.001
- [18] I. Oja, A. Mere, M. Krunks, C.-H. Solterbeck, M. Es-Souni, Properties of TiO₂ Films Prepared by the Spray Pyrolysis Method, *Solid State Phenomena* 99–100, 259 (2004). <https://doi.org/10.4028/www.scientific.net/SSP.99-100.259>
- [19] Xu Shiping, Xiang Sun, Yuan Gao, Min Yue, Qinyan Yue, Baoyu Gao, Solvent effects on microstructures and properties of three-dimensional hierarchical TiO₂ microsphere

- structures synthesized via solvothermal approach, *J. Solid State Chem.* 253, 167 (2017).
<https://doi.org/10.1016/j.jssc.2017.05.001>
- [20] M. Ge, J. Cai, J. Iocozzia, C. Cao, J. Huang, X. Zhang, J. Shen, S. Wang, S. Zhang, K.-Q. Zhang, Y. Lai, Z. Lin, A review of TiO₂ nanostructured catalysts for sustainable H₂ generation, *Int. J. Hydrogen Energy* 42 8418 (2017).
<https://doi.org/10.1016/j.ijhydene.2016.12.052>
- [21] W. Zhao, W. Wang, X. Feng, L. He, Q. Cao, C. Luan, J. Ma, Preparation and characterization of transparent indium-doped TiO₂ films deposited by MOCVD, *Ceram. Int.* 43, 8391 (2017). <https://doi.org/10.1016/j.ceramint.2017.03.182>
- [22] D.D. Marco, K. Drissi, P.M. Geffroy, N. Delhote, O. Tantot, S. Verdeyme, T. Chartier, Dielectric properties of alumina doped with TiO₂ from 13 to 73 GHz, *J. Eur. Ceram. Soc.* 37, 641 (2017). <https://doi.org/10.1016/j.jeurceramsoc.2016.09.016>
- [23] N.N. Bao, J.B. Yi, H.M. Fan, X.B. Qin, P. Zhang, B.Y. Wang, J. Ding, S. Li, Vacancy induced room-temperature ferromagnetism in Ga-TiO₂, *Scr. Mater.* 66, 821 (2012).
<https://doi.org/10.1016/j.scriptamat.2012.02.031>
- [24] Y. Gao, S. Thevuthasan, D.E. McCready, M. Engelhard, MOCVD growth and structure of Nb- and V-doped TiO₂ films on sapphire, *J. Cryst. Growth* 212, 178 (2000).
[https://doi.org/10.1016/S0022-0248\(00\)00010-5](https://doi.org/10.1016/S0022-0248(00)00010-5)
- [25] E.M. Samsudin, S.B. Abd Hamid, J.C. Juan, W.J. Basirun, A.E. Kandjani, S.K. Bhargava, Controlled nitrogen insertion in titanium dioxide for optimal photocatalytic degradation of atrazine, *RSC Adv.* 5, 44041 (2015). <https://doi.org/10.1039/C5RA00890E>
- [26] W. Choi, A. Termin, M.R. Hoffmann, The role of metal ion dopants in quantum-sized TiO₂: correlation between photoreactivity and charge carrier recombination dynamics, *J. Phys. Chem. C* 98, 13669 (1994). <https://doi.org/10.1021/j100102a038>
- [27] N.A. Al Saqri, A. Mondal, J.F. Felix, Y.G. Gobato, V.O. Gordo, H. Albalawi, D. Jameel, H. Alghamdi, F. Al Mashary, D. Taylor, M.S. Abd El-Sadek, M. Henini, Investigation of defects in indium doped TiO₂ thin films using electrical and optical techniques, *J. Alloy. Comp.* 698, 883 (2017). <https://doi.org/10.1016/j.jallcom.2016.12.294>
- [28] Biswajit Choudhury, Munmun Dey, Amarjyoti Choudhury, Defect generation, d-d transition, and band gap reduction in Cu-doped TiO₂ nanoparticles, *Int. Nano Lett.* 3, 25 (2013). <https://doi.org/10.1186/2228-5326-3-25>

- [29] M.R. Delsouz Khaki, M.S. Shafeeyan, A.A.A. Raman, W.M.A.W. Daud, Enhanced UV–Visible photocatalytic activity of Cu-doped ZnO/TiO₂ nanoparticles, *J. Mater. Sci. Mater. Electron.* 29, 5480 (2018). <https://doi.org/10.1007/s10854-017-8515-9>
- [30] A. Uhlir, Electrolytic shaping of germanium and silicon, *Bell Tech. J.* 35, 333 (1956). <https://doi.org/10.1002/j.1538-7305.1956.tb02385.x>
- [31] L.T. Canham, Silicon quantum wire array fabrication by electrochemical and chemical dissolution of wafers, *Appl. Phys.* 57, 1046 (1990). <https://doi.org/10.1063/1.103561>
- [32] A.I. Manilov, V.A. Skryshevsky, Hydrogen in porous silicon A review, *Mater. Sci. Eng., B* 178, 942 (2013). <https://doi.org/10.1016/j.mseb.2013.05.001>
- [33] C. Roy Chaudhuri, A review on porous silicon based electrochemical biosensors: beyond surface area enhancement factor, *Sens. Actuators B Chem.* 210, 310 (2015). <https://doi.org/10.1016/j.snb.2014.12.089>
- [34] Z. Huang, N. Geyer, P. Werner, J. de Boor, U. Gösele, Metal-Assisted chemical etching of silicon: a review, *Adv. Mater.* 23, 285 (2010). <https://doi.org/10.1002/adma.201001784>
- [35] P. Dwivedi, N. Chauhan, P. Vivekanandan, S. Das, D. Sakthi Kumar, S. Dhanekar, Scalable fabrication of prototype sensor for selective and sub-ppm level ethanol sensing based on TiO₂ nanotubes decorated porous silicon, *Sens. Actuators B* 249, 602 (2017). <https://doi.org/10.1016/j.snb.2017.03.154>
- [36] Y. Wang, Y.R. Su, L. Qiao, L.X. Liu, Q. Su, C.Q. Zhu, X.Q. Liu, Synthesis of one-dimensional TiO₂/V₂O₅ branched heterostructures and their visible-light photocatalytic activity towards Rhodamine B, *Nanotechnology* 22, 225702 (2011). 10.1088/0957-4484/22/22/225702
- [37] L. Wei, C. Yu, Q. Zhang, H. Liu, Y. Wang, TiO₂-based heterojunction photocatalysts for photocatalytic reduction of CO₂ into solar fuels, *J. Mater. Chem. A.* 6, 22411 (2018). <https://doi.org/10.1039/C8TA08879A>
- [38] G. Sahasrabudhe, S.M. Rupich, J. Jhaveri, A.H. Berg, K. Nagamatsu, G. Man, Y.J. Chabal, A. Kahn, S. Wagner, J.C. Sturm, J. Schwartz, low-temperature synthesis of a TiO₂/Si heterojunction, *J. Am. Chem. Soc.* 137, 14842 (2015). <https://doi.org/10.1021/jacs.5b09750>
- [39] T. Ji, Q. Liu, R. Zou, Y. Zhang, L. Wang, L. Sang, M. Liao, J. Hu, Enhanced UV-visible light photodetectors with a TiO₂/Si heterojunction using band engineering, *J. Mater. Chem. C.* 5, 12848 (2017). <https://doi.org/10.1039/C7TC04811D>

- [40] G. Santamaría-Juarez, E. Gomez-Barojas, E. Quiroga-González, E. Sanchez- Mora, J.A. Luna-Lopez, Oxidized porous silicon as a non-interfering support for luminescent dyes, *Mesoporous Biomater.* 3, 61 (2016). <https://doi.org/10.1515/mesbi-2016-0008>
- [41] E. Quiroga-Gonzalez, J. Carstensen, C. Glynn, C. O'Dwyer, H. Föll, Pore size modulation in electrochemically etched macroporous p-type silicon monitored by FFT impedance spectroscopy and Raman scattering, *Phys. Chem. Chem. Phys.* 16, 255 (2014). 10.1039/C3CP53600A
- [42] Q. Wu, D. Li, Z. Chen, X. Fuzhi, New synthesis of a porous Si/TiO₂ photocatalyst: testing its efficiency and stability under visible light irradiation, *Photochem. Photobiol. Sci.* 5, 653 (2006). <https://doi.org/10.1039/B517744H>
- [43] R. Liu, W. Li, T. Cai, Y. Deng, Z. Ding, Y. Liu, X. Zhu, X. Wang, J. Liu, B. Liang, T. Zheng, J. Li, TiO₂ nanolayer-enhanced fluorescence for simultaneous multiplex mycotoxin detection by aptamer microarrays on a porous silicon surface, *ACS Appl. Mater. Interfaces* 10, 14447 (2018). <https://doi.org/10.1021/acsami.8b01431>
- [44] N. Baran, H. Gebavi, L. Mikac, D. Ristic, M. Gotic, K.A. Syed, M. Ivanda, Sensing properties of oxidized nanostructured silicon surface on vaporized molecules, *Sensors* 19, 119 (2019). <https://doi.org/10.3390/s19010119>
- [45] S. Oussidhoum, D. Hocine, D. Chaumont, A. Crisbasan, M. Bensidhoum, E. Bourennane, A. Moussi, E. Lesniewska, N. Geoffroy, M.S. Belkaid, Optimization of physicochemical and optical properties of nanocrystalline TiO₂ deposited on porous silicon by metal-organic chemical vapor deposition (MOCVD), *Mater. Res. Express* 6, 125917 (2019). <https://doi.org/10.1088/2053-1591/ab6539>
- [46] F.N. Fahrizal, M.K. Ahmad, N.M. Ramli, N. Ahmad, R. Fakhriah, F. Mohamad, N. Nafarizal, C.F. Soon, A.S. Ameruddin, A.B. Faridah, M. Shimomura, K. Murakami, Fabrication of TiO₂ nanostructures on porous silicon for thermoelectric application, *AIP Conf. Proc.* 1883, 20031 (2017). <https://doi.org/10.1063/1.5002049>

CHAPTER 2

METHODOLOGY

Different experiments were carried out with the aim of identifying the differences in the morphology and structure of the TiO₂, depending on the synthesis conditions, when prepared by the solvothermal route.

The chemicals used in this work were of reagent grade. Hydrofluoric acid 48% (HF) was provided by MERCK, hydrogen peroxide (H₂O₂), hydrochloric acid (HCl), and methanol (CH₃OH) were provided by J.T. Baker. Silver nitrate (AgNO₃), titanium butoxide, and copper chloride (CuCl₂) were provided by Sigma-Aldrich, and finally, the indium chloride hydrate (InCl₃H₂O) was provided by Alfa Aesar.

The MACE method was used to prepare PS from single-side polished (100) p-type Si wafers with $\rho = 15\text{--}25 \text{ }\Omega\text{cm}$ and $675 \pm 20 \text{ }\mu\text{m}$ of thickness. Before the chemical etching, the Si wafers were cleaned with deionized water/hydrofluoric acid (HF) (3:1) for 30 s and rinsed with deionized water to remove the native oxide film. Then, the wafers were cleaned in acetone for 5 min in an ultrasonic bath and rinsed again with deionized water, and finally, these wafers were dried with nitrogen. MACE was carried out using Ag nanoparticles as a catalyst, which were deposited on the Si substrates using an AgNO₃ aqueous solution of 0.002 M. The plating solution contained 50 mL of the aqueous solution of AgNO₃, 1.75 mL of H₂O₂, and 1 mL of HF (48% purity). Pieces of Si were immersed in the plating solution for 30 s at room temperature and in an ultrasonic bath. After depositing the Ag nanoparticles, the Si substrates were rinsed with deionized water to remove the excess of Ag. Immediately after this process, the Si substrates were immersed in the etching solution for 30 min. This

etching solution contained 50 mL of deionized water, 7 mL of H₂O₂, and 4 mL of HF (48% purity). The product of this process was a PS layer on the surface of the Si substrates. After etching, the samples were rinsed with deionized water and dried with nitrogen gun.

TiO₂ was synthesized by the solvothermal method using titanium butoxide as the precursor at 180 °C by 4 h (Figure 1a shows schematics of the preparation methods). This method was used to synthesize the TiO₂ particles and most of them grow on the walls of the PS layer and on the surface. This investigation does not try to fill the pores, only growing TiO₂ particles in the pore walls. In the literature, the TiO₂ synthesis has been performed varying the type of solvent. In this work, the precursor concentration was also varied. Hydrochloric acid (HCl) was used to add acidity to the medium (it is common to obtain nanoparticles instead of bigger particles when working in acidic medium), and ethylene glycol (HOCH₂CH₂OH), methanol (CH₃OH), and acetone (CH₃COCH₃) were employed as solvents. For the synthesis, four experimental procedures were used: in the first one, the titanium butoxide concentration was varied. The amount of this substance was 2, 0.25, and 0.083 mL for the experiments. It was mixed with 1 mL of HCl and dissolved in 10 mL ethylene glycol (used as solvent) in a Teflon-lined autoclave with a capacity of 15 mL under magnetic stirring for 5 min, and then a small piece of PS was introduced before closing it. Then, the autoclave was introduced into the furnace at 180 °C for 4 h. The second experimental procedure consisted in varying the type of solvent. 0.083 mL of titanium butoxide and 1 mL of HCl were dissolved in 10 mL of ethylene glycol, methanol, or acetone, under the same conditions previously mentioned. The third procedure consisted in dissolving 0.083 mL of titanium butoxide and 1 mL of HCl in 10 mL of methanol together with 6 mMol of copper II chloride (CuCl₂) and repeating the same steps as the first experiment. The fourth procedure was equivalent to the previous

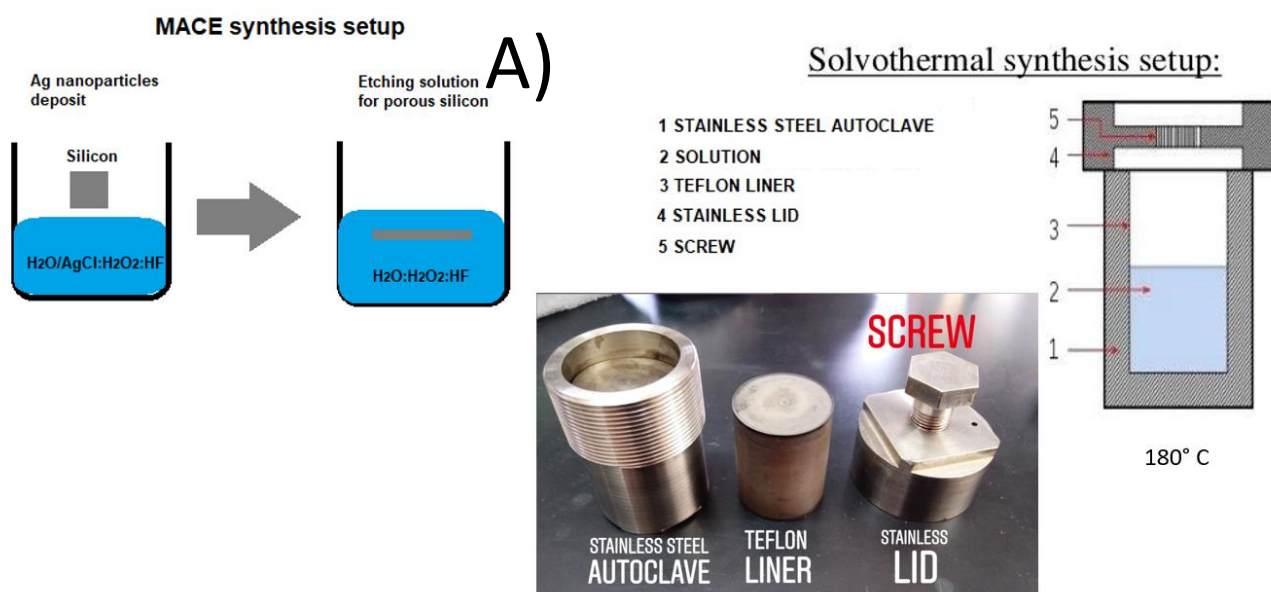
experiments; the only difference was the dopant, which in this case was 6 mMol of indium III chloride dissolved in methanol. After following the above-mentioned synthetic procedures Cu and In doped TiO₂ were obtained.

After taking the autoclaves out of the oven, they were left to cool down naturally at room temperature. The samples were rinsed with deionized water and dried with nitrogen. Finally, the samples were thermally treated at 400 °C for 3 h under an air environment. This thermal treatment works only to improve the TiO₂ crystallinity. The indium salt is introduced for doping TiO₂. This temperature is insufficient to generate doping in the PS. It is possible that some indium emigrates to the PS, but the temperatures are low, and the Indium doping for the PS requires high temperatures for the diffusion process.

Table 1 lists the samples prepared under different conditions. In order to obtain the electrical characteristics, nickel circular contacts (1mm diameter and 500 nm of thickness) were deposited on top of the structures, whereas Al contacts were deposited at the bottom side of the heterostructures (500 nm of thickness) by high vacuum evaporation. Finally, the heterostructures were thermally treated at 400 °C for 30 min to improve the adherence between the sample and the metal contacts; a higher temperature could degrade the heterostructures. In Figure 1b, the heterostructure of the device is depicted. It consists of PS with TiO₂ nanoparticles deposited on its pore-walls, and with Ni and Al contacts.

Table 1. Samples prepared under different conditions

Sample	Precursor Solution	Proportion (V: V: V) mL
PTI01 (High glycol)	Titanium butoxide: Ethylene glycol (EG)	HCl: 2:1:10
PTI02 (Medium glycol)	Titanium butoxide: Ethylene glycol (EG)	HCl: 1:4:40
PTI03 (Low glycol)	Titanium butoxide: Ethylene glycol (EG)	HCl: 1:6:60
PTI04 (Methanol)	Titanium butoxide: Methanol (M)	HCl: 1:6:60
PTI05 (Acetone)	Titanium butoxide: Acetone (A)	HCl: 1:6:60
PTICu (Methanol+Cu)	Titanium butoxide: Methanol:CuCl ₂	HCl: 1:6:60+6mMol
PTIIn (Methanol+In)	Titanium butoxide: Methanol:InCl ₂	HCl: 1:6:60+6mMol



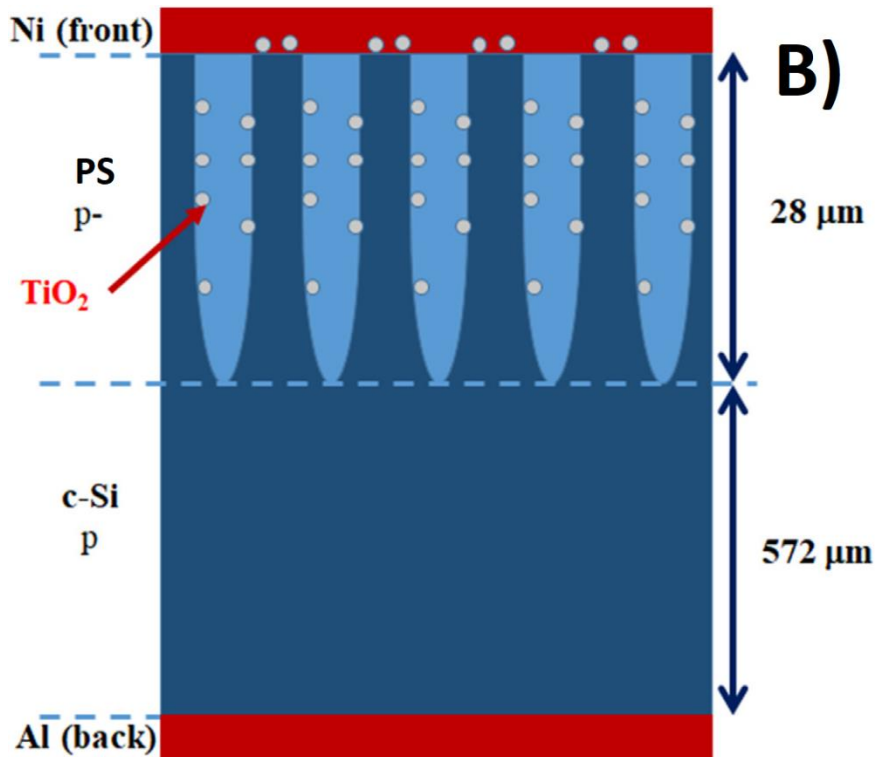


Figure 1. a) Preparation methods for porous silicon and TiO_2 b) Schematic of a TiO_2/PS heterostructure studied in this work. The upper elongated figures represent the pores in Si (forming PS).

The samples were characterized using Field-Emission Scanning Electron Microscopy (FE SEM) using a FEI-SCIOS DualBeam equipment to observe the morphology of the Ag nanoparticles and to analyze in cross-section and top-view the structure of the PS layers before and after depositing the TiO_2 material. Moreover, the samples were not coating with any conductor layer and the SEM images were recorded with the secondary electrons method. Raman spectra of the samples were recorded using a Horiba Raman LabRam HR microscope, with a 632 nm laser using a 50x magnification.

XRD diffractograms were obtained by using two systems. First, a Panalytical-Empyrean diffractometer with $\text{Cu K}\alpha$ radiation ($\lambda=0.15418$ nm). The TiO_2 powder diffractograms were recorded in the 2θ range from 10° to 70° at a scan rate of 0.017° step size. Additionally, a D8

discover Bruker diffractometer, operated at 40 kV and 40 mA using the $\text{CuK}\alpha 1$ radiation (1.5406 Å). The TiO_2 powder diffractograms were recorded from 20° to $80^\circ 2\theta$ in 0.04° steps. Room temperature diffuse reflectance spectra of the heterostructures were measured using a Cary 5000 UV–vis–NIR system (Agilent Technologies Inc., Santa Clara, CA, USA). The reflectance spectra were recorded in a range from 200 to 1500 nm with a resolution of 1 nm. The photoluminescence (PL) response was measured at room temperature using a Horiba Jobin Yvon spectrometer model FluoroMax 3 (Edison, NJ, USA) with a pulsed xenon excitation source and a multiplier tube detector controlled by a computer. The samples were excited using radiation of 330 nm, and the luminescence response was recorded in a range from 370 to 1000 nm with a resolution of 1 nm.

Current-voltage (I-V) and current-time (I-t) characteristics were measured with a Keithley 4200A-SCS Parameter Analyzer. The I-V curves were recorded from negative to positive voltages at a voltage sweep rate of 1.4 V/s. The current was limited to 10 mA to avoid damaging the devices.

CHAPTER 3

RESULTS AND DISCUSSION

3.1 Morphological characterization

Ag nanoparticles were homogeneously deposited on Si substrates showing spherical shapes and narrow particle size distribution, as can be seen in Figure 2. The Ag nanoparticles diameter varies from 8 to 34 nm (see the inset image in Figure 2), something interesting in Figure 2 is the formation of some cavities. During Ag deposition, H_2O_2 is reduced by the catalytic effect of Ag, liberating holes, which are needed for the etching process (to produce SiO_2 , which is dissolved by HF) [1, 2]. The most accepted mechanism for the deposition of metallic Ag is the oxidation and dissolution of the Si substrate first, and the most suitable mechanism for this is a direct dissolution of Si in a tetravalent state, when the HF reacts with either Si or SiO_2 , producing H_2SiF_6 and liberating electrons. These electrons reduce the Ag^+ ions from AgNO_3 generating Ag^0 on the surface of the Si substrate [1, 2].

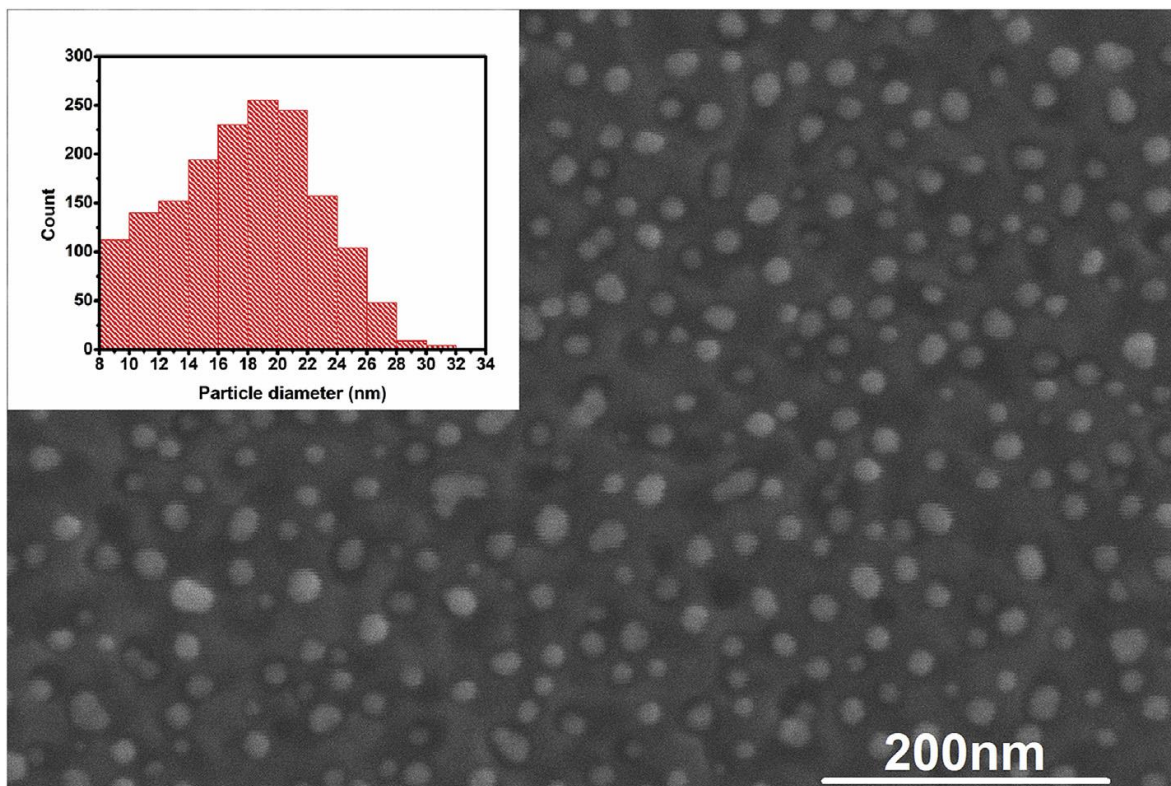


Figure 2. SEM micrograph of Ag nanoparticles deposited on silicon substrates.

Figure 3 shows the top and cross-section views of the PS layers synthesized by MACE. A sponge-like structure very identical to the PS obtained using the conventional electrochemical anodization process is observed in Figure 3a. It is possible to observe a circular cross-sectional shape of the pores. The pore size is bigger than the nanoparticle size, above 100 nm. According to the IUPAC classification, these pores are in the macropore category [3]. The significant difference between the pore and nanoparticle sizes is evident, and it is caused by the merging of the nearest pores upon etching.

According to Huang et al. [1], the MACE process can be described considering five steps: 1) the oxidant is reduced at the surface of the metal particle. 2) The holes liberated by the reduction of the oxidant diffuse through the metal and are injected into Si. 3) The injected holes oxidize and dissolve the Si atoms at the interface Si/Ag by HF. 4) The concentration of

holes is the highest at the interface between Si and metal. Therefore, the Si that is in contact with the Ag metallic is etched much faster by HF than a bare Si surface without metal coverage. 5) The holes diffuse from the Si under the noble metal to off-metal areas or the wall of the pore if the rate of hole consumption at the Si/metal interface is lower than the rate of hole injection. Figure 3b shows a cross-section of the PS layer where Si channels can be observed (the inset image in Figure 3b shows a zoom-in of this structure). It can be observed in two regions in the PS layer, the first region has a thickness of around 8 μm , and the second region has a thickness of around 20 μm . This phenomenon is rarely seen, and we could attribute it to the nature of the chemical etching since the highest concentration of Ag nanoparticles reach a limit at a specific region where the fifth step previously mentioned is inverted. The total thickness of the porous silicon layers is around 28 μm at 30 min, which indicates that the etching rate is around 0.93 μm per minute.

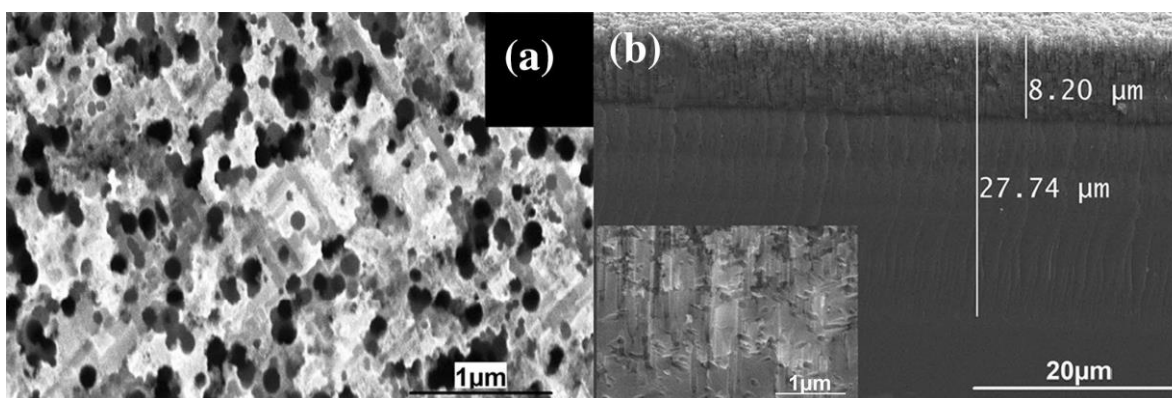


Figure 3. SEM micrographs of the PS in a) top view b) cross-section

Figure 4 shows the top view and cross-section of the samples of TiO_2/PS , varying the titanium butoxide concentration and the solvent. Figure 4a and b shows TiO_2 on the PS synthesized with 2:1:10 of titanium butoxide, HCl, and ethylene glycol in volume ratio, respectively. A disordered morphology of loosely packed flocs assembled from 2D

nanosheets with irregular shapes can be observed, and same 2D structures have been reported by Xu et al. [4]. Nanosheets fully cover the PS surface, even blocking the view of silicon pores. Nevertheless, the cross section shows some pores with a partial infiltration of TiO₂ agglomerates.

This can be attributed to the size of these agglomerates, which is bigger than the pore diameter; moreover, the surface tension and the viscosity of the ethylene glycol may affect capillary pressure and absorption capacity of the solution, allowing wettability conditions into the pores.

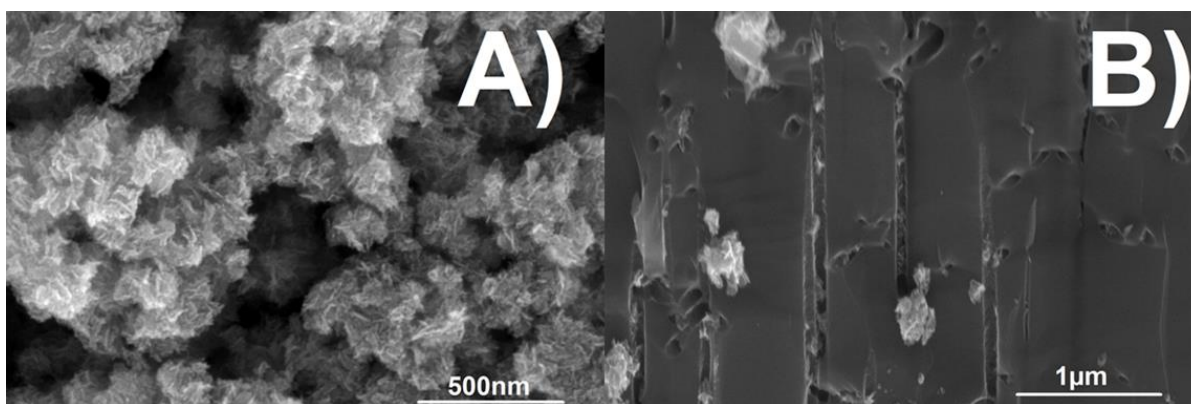


Figure 4. SEM micrographs in top view and cross-section of TiO₂ on PS **a)** top view PTI01, **b)** cross-section PTI01.

Figure 4c and d shows the TiO₂ structures synthesized with 1:4:40 of titanium butoxide, HCl, and ethylene glycol in volume ratio, respectively, in top view and cross-section.

Figure 4c shows that TiO₂ morphology and size change considerably compared to the first case (2:1:10) since it can be observed spheres with a regular structure and a well-defined shape. These spherical structures seem to be as TiO₂ agglomeration of short nanorods. This effect is contradictory to what is mentioned by Xu et al. [4], where they mentioned that using ethylene glycol constitutes the formation of irregular structures without distinct shape building blocks. Another interesting thing observed is the spherical structure that possesses

a comparable size to the pores, or even smaller than the pores, which allows the introduction of the spheres inside of the pores as it can be seen in Figure 4c. Figure 4d shows a cross section to corroborate the introduction of these spheres. However, as can be seen, only some spheres can be noticed; this could be because the size of the TiO_2 structures is comparable with the pore size, which generates a bottleneck along the channel. Thus, the introduction of TiO_2 particles along the Si channel is inhibited.

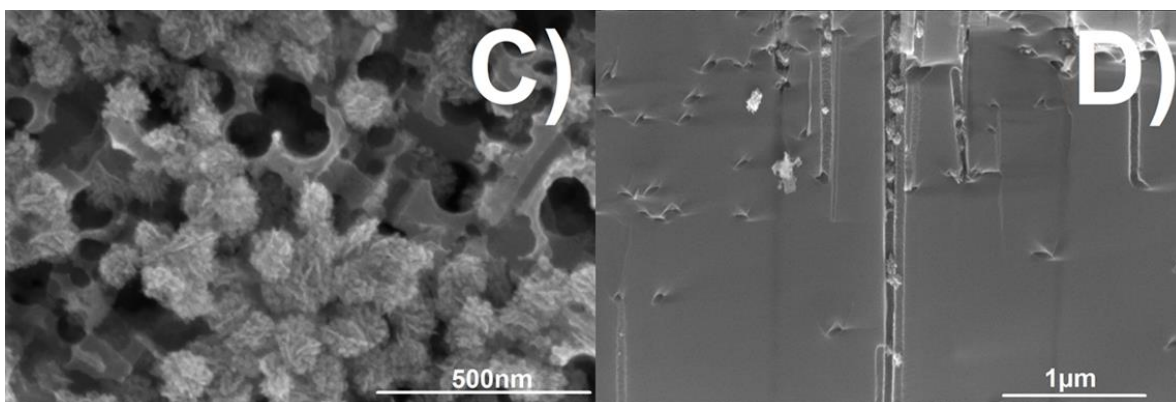


Figure 4. SEM micrographs in top view and cross-section of TiO_2 on PS **c)** top view PTI02, **d)** cross-section PTI02.

Figure 4e and f shows the top view and cross-section FESEM images of TiO_2 structures synthesized with 1:6:60 of titanium butoxide, HCl, and ethylene glycol in volume ratio, respectively. Figure 4e presents a new morphology concerning the previous experiments shown. In this case, the size of the agglomerates decreases considerably, and the spherical form remains unchanged as in the second case (1:4:40, Figure 4c and d). TiO_2 nanospheres decorate the PS surface. In Figure 4f, the cross-section shows the pores with nanospheres decorating along the Si channel. Hence, it is demonstrated that titanium butoxide concentration plays an important role in morphology and size control. Since, in the first case (2:1:10), the morphology turns out to be nanosheets or nanoflakes, in the second case (1:4:40)

the morphology seems to be short nanorods, and in the third case (1:6:60 volume ratio) the morphology drives to the agglomeration of nanoparticles.

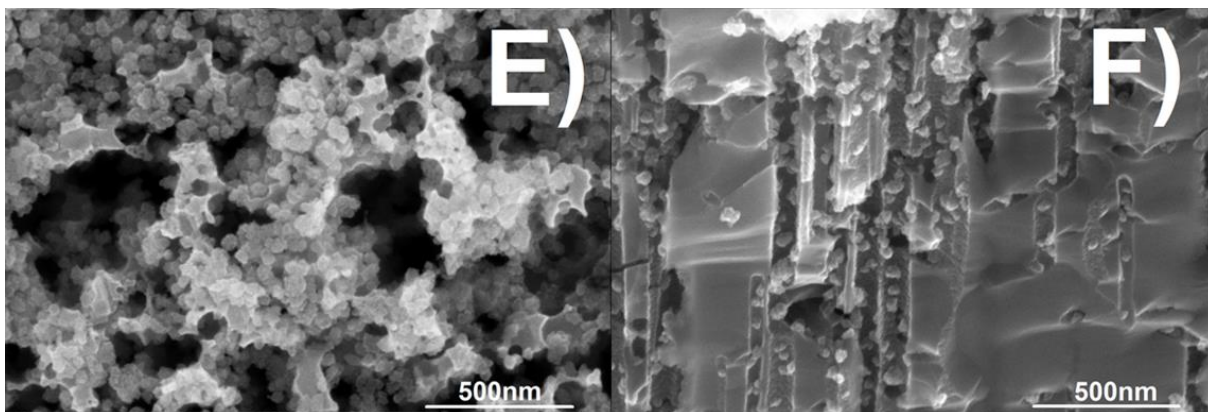


Figure 4. SEM micrographs in top view and cross-section of TiO₂ on PS e) top view PTI03, f) cross-section PTI03.

Figure 4g and h shows the top view and cross-section FESEM images of TiO₂ structures synthesized under the following conditions: 1:6:60 of titanium butoxide, HCl, and methanol volume ratio, respectively. According to the top view FESEM image (Figure 4g), a radical change in comparison with the other experiments can be observed; in this case, the formation of TiO₂ regular nanoparticles (size ~ 15 nm) is evident; this morphology is slightly identical to Figure 4e. However, size is smaller than using ethylene glycol. Likewise, it can be noticed that nanoparticles cover the fulfill surface of the PS and the Si channels; this coating is a conformal deposit. Figure 4h shows the cross-section of the sample with 1:6:60 of titanium butoxide, HCl, and methanol volume ratio. Figure 4h corroborates the coating of the Si surface and channels by TiO₂ nanoparticles like a conformal deposit. It is well known that sophisticated processing methods only reach conformal deposits such as sputtering, ALD, plasma, or PECVD [5-8].

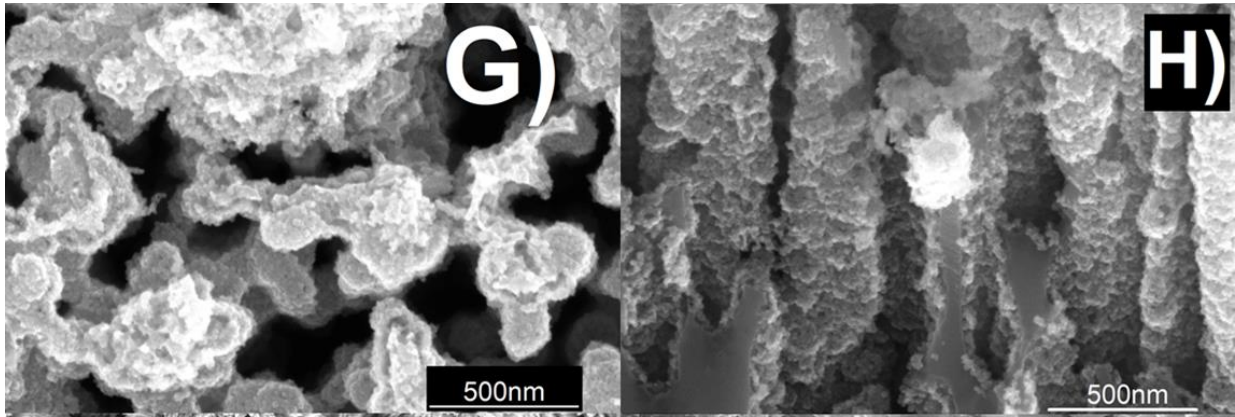


Figure 4. SEM micrographs in top view and cross-section of TiO_2 on PS **g)** top view PTI04, **h)** cross-section PTI04.

Finally, Figure 4i and j shows the top view and cross-section images of TiO_2 structures synthesized with 1:6:60 of titanium butoxide, HCl, and acetone volume ratio, respectively.

Figure 4i shows micro-flower structures composed of a large number of nanorods along the radial direction from the core to the surface. Something similar has been reported by Xu et al. [4] with identical sizes. Figure 4j shows the cross-section of the TiO_2 /PS sample; however, because the size of these micro-flowers is ten times bigger than the pore size, the insertion of these TiO_2 structures was impossible.

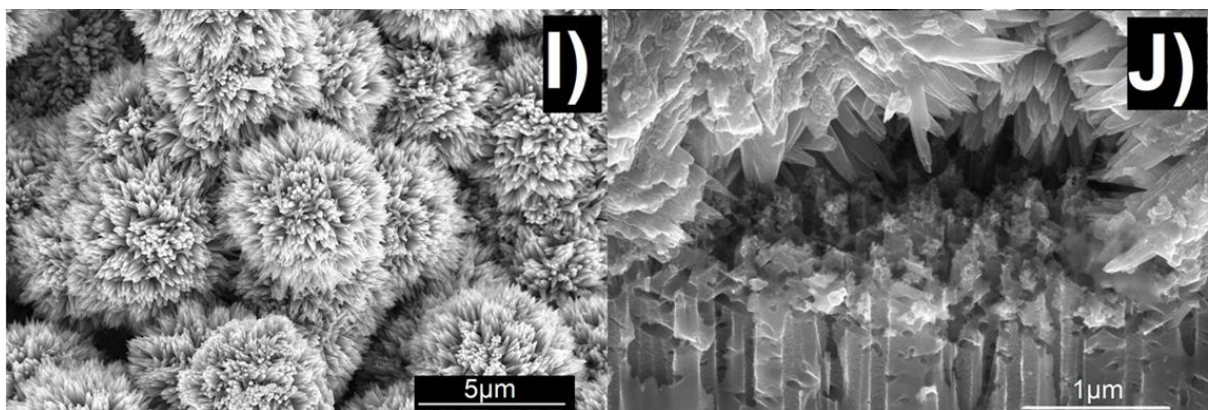


Figure 4. SEM micrographs in top view and cross-section of TiO_2 on PS **i)** top view PTI05, **j)** cross-section PTI05.

The morphology observed in SEM images clearly shows a tendency both changing the alkoxide concentration and varying the solvent. The variation of butoxide concentration results in the morphology and size structures from bigger (agglomeration of nanosheets with the highest concentration) to smaller structures (nanospheres and nanoparticles with the lowest concentration). Moreover, the change of the solvent results in the variation of the morphology or size.

The EG solvent generates irregular nanoparticles of around 50 nm, and the M solvent promotes the formation of perfect nanoparticles of approximately 15 nm. However, the A solvent creates a change in morphology and size as urchin-like micrometric structures. Therefore, the concentration of the titanium precursor and solvent variation can modify the morphology and size of the TiO₂ structures.

On the other hand, in Figures 4k and 4l show the TiO₂:Cu/PS heterostructures in a top and cross-section views. This sample displays a radical change in the morphology in comparison with the non-doped sample (4g and 4h). In this case, two morphologies can be observed, the first one corresponds to irregular nanoparticles with a same size to the pores, and therefore, these particles can enter the pores. In the second, the morphology has a peculiar form identical to a cauliflower of micrometric size (as it is shown in the inset image of Figure 4k). Multiple agglomerations of short nanorods form this structure from the core to the surface. The change of the morphology is due to the segregation of Cu (even at low concentrations) which could be similar to that reported for copper thin films [9]. Figure 4l shows the cross-section of the heterostructure, and some TiO₂ particles inside of the Si channels can be seen. The particle size is comparable to the pore size. Therefore, it is difficult to achieve full decoration of the Si channels (as can be seen in Figure 4h).

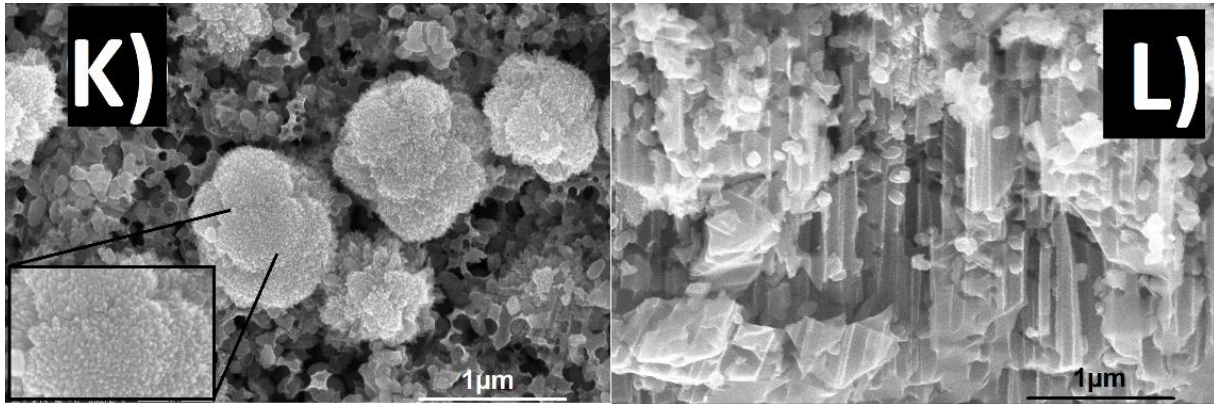


Figure 4. SEM micrographs in top view and cross-section of TiO_2 on PS **k)** top view PTICu, **l)** cross-section of PTICu.

Figure 4m and 4n shows the TiO_2 :In/PS heterostructure in top and cross-section views. Figure 4m shows a similar morphology as in the non-doped case (4g and 4h). However, there are many changes in morphology. First, the size of these particles increases almost two times; it can be seen in Figure 4g. Second, by comparing Figure 4g and 4m, it can observe that there is a more significant agglomeration in the TiO_2 : In sample than in pure TiO_2 (Figure 4g), the PS surface seems to disappear because of the coating. Third, the geometry of these particles changes from spherical (non-doped TiO_2) to cubic forms (In-doped TiO_2 and the inset image in Figure 4m shows this morphology). The TiO_2 structures morphology doped with In are affected as in the Cu-doped TiO_2 case. Figure 4n shows the cross-section of the heterostructure, and it observes how the In doped TiO_2 nanoparticles fill the Si channels. This effect is different in comparison with the non-doped TiO_2 sample (which can be considered as a conformal deposit).

The images confirm that the doped radically affects the TiO_2 morphology, even if low concentrations are used. Therefore, it could be considered an effective way to modify the morphological properties of the TiO_2 instead of changing solvents [4]. Moreover, doped TiO_2

structures not only change in their morphology but also in their optical, structural, and electrical properties, and this can be taken to our advantage.

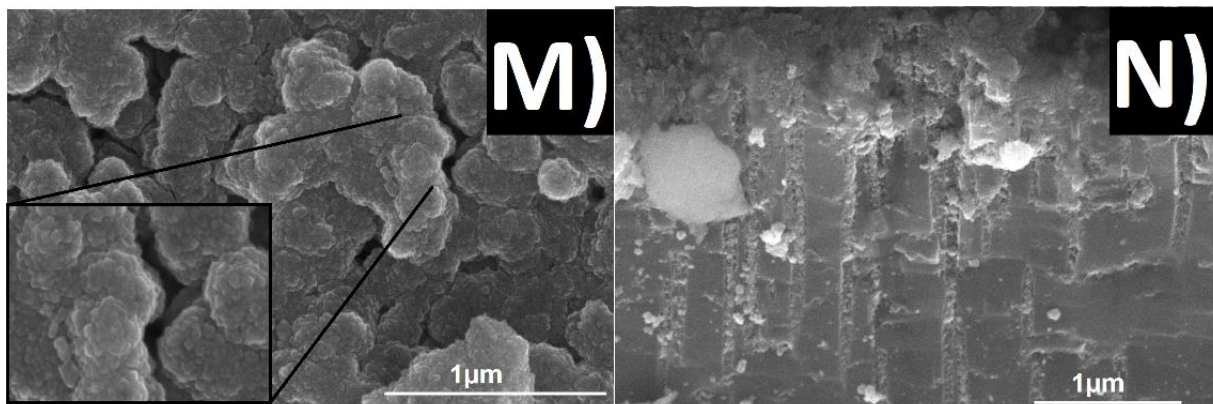


Figure 4. SEM micrographs in top view and cross-section of TiO₂ on PS **m)** top view PTIn, **n)** cross-section PTIn.

3.2 Structural and compositional characterization

Figure 5 shows the XRD patterns corresponding to TiO₂ structures obtained under different processing conditions. As can be observed in Figure 5a, the samples PTI01, PTI02, PTI03, and PTI04 show the characteristic peaks of TiO₂ around 25.36°, 37.88°, 48.09°, 53.99°, 55.01°, and 70.47° 2θ , associated with (101), (004), (200), (105), (211), and (220) planes, respectively. These peaks confirm that the predominant phase is the tetragonal anatase, being in good agreement with the report of [10]. However, two additional peaks found around 62.74° and 68.97° can be easily confused between the anatase and the rutile phase, due to the closed position between peaks. However, the main peak around 25.36° correspond to the anatase phase, therefore is impossible that these peaks correspond to the rutile phase. The peak around 62.74° is the (204) plane of anatase and the peak around 68.97° correspond to the (116) plane of anatase. On the other hand, sample PTI05 shows peaks distinctive of the

rutile phase, around 27.51° , 36.1° , 39.13° , 41.28° , 44.01° , 54.35° , and 56.5° 2θ , which correspond to (110), (101), (200), (111), (210), (211), and (220) planes, respectively. Samples tend to form monophasic TiO_2 structures (rutile). The peak around $68-70^\circ$ is a problem presented due to the silicon substrate that generates an intense signal that overshadows the rest of the signal. For that reason, the XRD signal of this samples was cut.

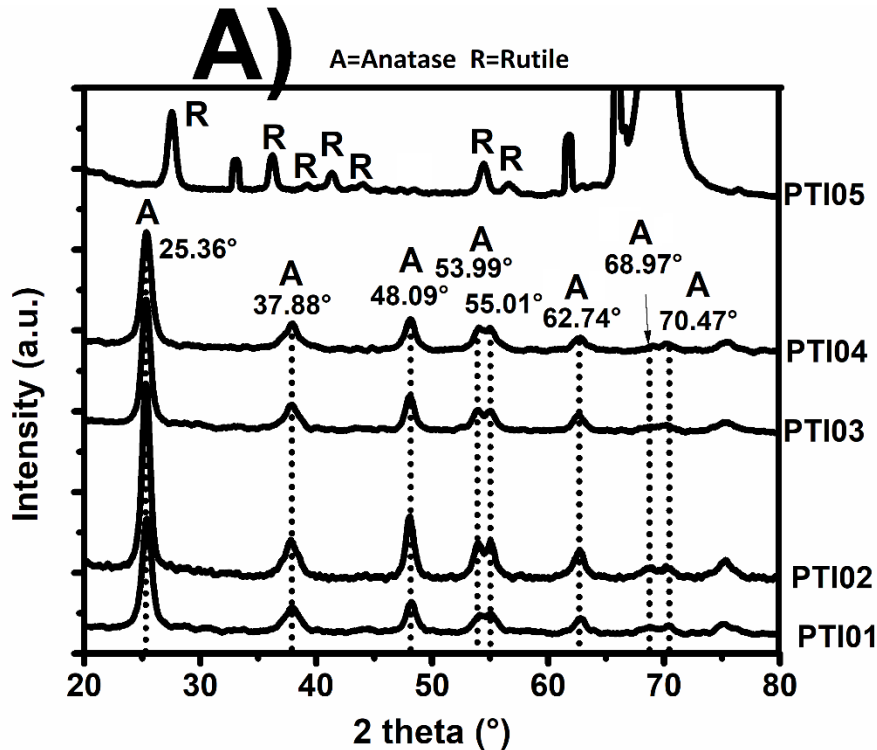


Figure 5. a) XRD patterns of un-doped samples under different conditions. A=Anatase R=Rutile

Figure 5b shows the XRD patterns of doped TiO_2 structures.

The sample PTICu (Cu doped) has almost the same peaks as in the previous case, with a slight shifting in 2θ . These peaks are positioned around 25.48° , 37.97° , 48.21° , 54.14° , 55.21° , and 62.93° , which are assigned to the anatase phase. Moreover, other peaks localized at 27.57° (110), 36.22° , and 41.39° can be considered as rutile phase peaks [11]. However, Choudhury et al. [12] consider these peaks as characteristic of the brookite phase, but this

does not seem to be logical in our case. Since a thermal annealing was given in these samples; therefore, the brookite phase must disappear.

The PTIIIn sample (In doped) shows a shift in the position peaks in a similar fashion to that of the previous sample. The peaks localized around 25.51° , 37.99° , 48.32° , 54.1° , 55.29° , and 62.94° correspond to the anatase phase. All samples show the same peak positions, and the diffraction peak absence related to compounds derived from Indium or Copper can indicate three possibilities. The first one is that In and Cu ions have been incorporated into the TiO_2 lattice, i.e., there is not a synthesis of In or Cu composites in the TiO_2 structure as will be confirmed by Raman spectra. The second one suggests that these species were highly dispersed over the TiO_2 surface, and the third one, probably due to the low concentration of dopant [3]. In the literature [13, 14] there is a discussion if the In^{3+} or Cu^{2+} or other ions substitute the Ti^{4+} ion because of the larger radius of these dopant ions (0.81 \AA [14], and 0.73 \AA [12], respectively) compared to the Ti^{4+} radius (0.68 \AA [14]).

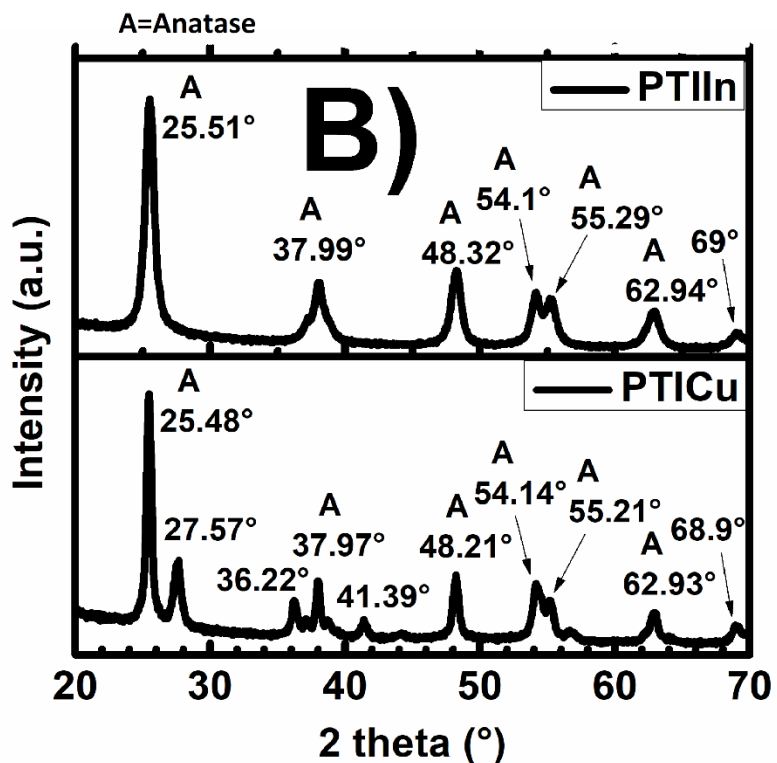


Figure 5. b) XRD patterns of In, Cu doped TiO_2 structures. A= Anatase.

Figure 6 shows the Raman spectra for the samples obtained under different synthesis conditions. Raman spectroscopy was used to determine the TiO_2 phase of the samples according to the position of the peaks [15–21]. Figure 6a shows the Raman spectra of the different samples un-doped. Sample PTI01 shows peaks at 144 cm^{-1} [16, 18, 21], 196 cm^{-1} [17, 21], 397 cm^{-1} [18, 20, 21], 516 cm^{-1} [17, 18, 21], and 638 cm^{-1} [18, 21] which have been catalogued for anatase phase and can be assigned as the E_g , B_{1g} , A_{1g} , B_{1g} modes. Samples PTI02 and PTI03 show the peaks at 143.9 cm^{-1} [16, 18, 21], 226.9 cm^{-1} [21] 434.9 cm^{-1} [16], 620 cm^{-1} and 623 cm^{-1} [15, 16] which indicate a combination of anatase and rutile phases. Sample PTI04 shows peaks at 146 cm^{-1} (E_g) [16, 18, 21], 228.1 cm^{-1} [21], 432.1 cm^{-1} [16] and 642 cm^{-1} (B_{1g}) [18] that characterize the anatase phase.

Finally, sample PTI05 shows the peaks around 144.7 cm^{-1} [16, 18, 21], 231.1 cm^{-1} (E_g) [21], 448.2 cm^{-1} (E_g) [17], and 608.8 cm^{-1} ($A1_g$) [17, 19] which correspond to the rutile phase. Mode E_g is due to the symmetric stretching vibration of O–Ti–O, the $B1_g$ mode is originated from the symmetric bending vibration of O–Ti–O, and the mode $A1_g$ corresponds to the antisymmetric bending vibration of O–Ti–O in TiO_2 [16].

According to Raman, the spectra, significant differences among the samples regarding their crystalline phase can be observed. This is strongly related to the synthesis conditions; for example, sample PTI01 synthesized with a high titanium butoxide concentration shows the characteristic peaks for a pure anatase phase. The anatase phase could give the morphology (flake-like). Samples PTI02 and PTI03 show the same peaks almost in the same position; however, they indicate a combination of anatase and rutile phases. The combination of these phases could be related to the morphology of the TiO_2 structures; SEM images (Figure 4) exhibit radical changes in the morphology of the samples from nanosheets (PTI01) to short nanorods (PTI02), and elongated nanoparticles (PTI03) can be observed. Sample PTI04 (methanol solvent) has almost a pure anatase phase with a peak related to the rutile phase. Meanwhile, the sample PTI05 (acetone solvent) shows almost a pure rutile phase. The combination of phases could be attributed to predominance in the agglomeration dimensionality. Reference [4] mentions that nanorods have a rutile phase, while the anatase phase is observed in nanosheets and other irregular morphologies.

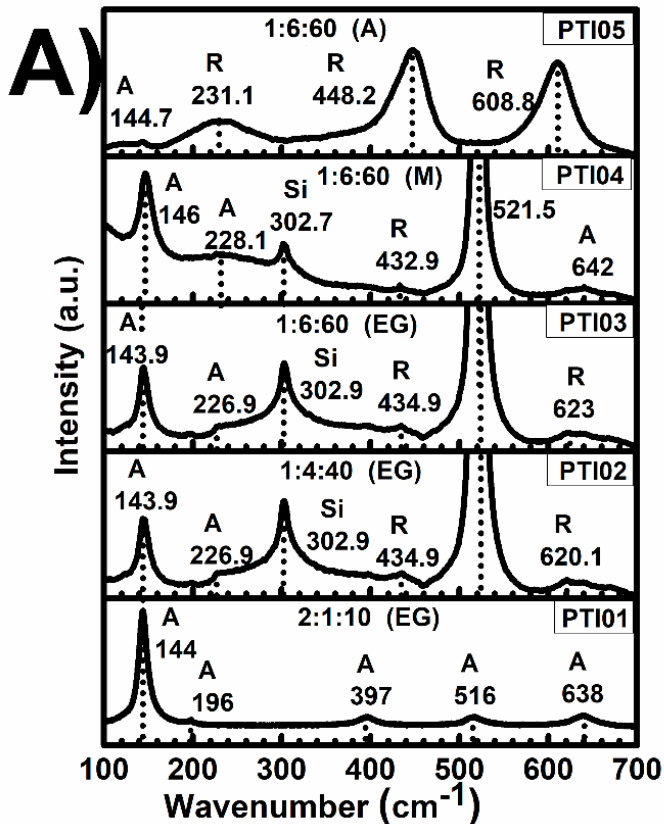


Figure 6. a) Raman spectra of TiO₂/PS structures un-doped

Also, it is important to note the predominance of the rutile phase when acetone is used. According to the literature [4], a good interface, which could separate the titanium precursor from the aqueous phase, is the key to control the formation of 3D structures, due to the control of the hydrolysis and polycondensation. The control of the morphology is the key to the predominant phase, as it was previously mentioned. Moreover, Zakrzewska [22] mentions that oxygen nonstoichiometry created at high sputtering rates promotes rutile growth. For that reason, the oxygen and the morphology could be the cause of the rutile phase formation. However, Xu et al. [4] mention that the solvent is the main promotor to generate 3D structures. The 3D structures are a result of the solvent properties such as polarity, boiling point, surface tension, dielectric constant, and more. Xu et al. [4] explain the effect of the

combination of the solvent, the acid medium, and the precursor. In this explanation, the dielectric constant reflects the solvent polarity, HCl is soluble in some polar solvents, and the titanium butoxide is soluble in only organic solvents. A high concentration of H^+ and Cl^- at the interface promotes the formation of the rutile phase, and the selective adsorption of Cl^- ions on the rutile (110) plane creates the growth along [001] direction to form rutile nanorods. Therefore, Xu et al. [4] inferred that an excellent liquid–liquid interface isolates the precursor agent from the aqueous phase and concentrates HCl. Therefore, using acetone makes a good interface, which is favorable for the formation of the quasi-3D urchin-like hierarchical microsphere structures. In the resume, the phase of the TiO_2 is related to the structure (3D agglomerates due to 1D structures), and the structure is connected with liquid–liquid interface of the elements in the solution.

On the other hand, Figure 6b shows the Raman spectra of the TiO_2/PS heterostructures with the different dopants used. Raman is a useful analytical technique to identify the phase in the TiO_2 structures tracking the peak position, as well as understanding the local change in the structure after the incorporation of dopant ions [12]. The sample PTICu in Figure 6b almost shows the same peak position with a slight shifting as a result of doping. However, it is not possible to observe any secondary peaks related to Cu or its oxide phases, as is reported by Choudhury et al. [12]. These peaks are positioned at 147cm^{-1} (E_g) [16, 18, 21], 228.5 cm^{-1} (E_g) [21], 434.2 cm^{-1} (E_g) [16], and 621.2 cm^{-1} (E_g) [16], which are characteristic of anatase and rutile phases. The incorporation of Cu ions in the heterostructure causes the shifting exhibited in the spectra, which in turn, is due to the difference in the ionic size of both metallic ions, 0.73 \AA for Cu^{2+} and 0.64 \AA for the Ti^{4+} . This difference causes a mismatch in the lattice structure. In addition, there is a valence difference between Cu(II) and Ti(IV); this affects the

stoichiometry of the Cu-doped TiO₂ to maintain the charge neutrality: the generation of oxygen vacancies [12]. In order to understand this effect, Cu²⁺ ions may substitute the Ti⁴⁺ ions, which generates a new bond in the lattice, this new bond could be Cu–O–Ti or Cu–O–Cu as it is claimed by Choudhury et al. [12]. The formation of these bonds will affect the Raman-active modes resulting in the shifting observed in the spectra. Choudhury et al. [12] mentioned that the E_g peak is associated with the Cu–O–Cu stretching mode vibration, and after doping, the vibration strength decreases due to the creation of oxygen vacancies nearby. Then, the lattice contracts due to the oxygen vacancies; therefore, the peak is shifted to a higher wavenumber [12].

However, the quantum size effect has been analyzed, which indicated to be an important parameter in the broadening and peak shifting [12, 23].

The sample PTIn shows shifting peaks around 148 cm⁻¹ (E_g) [16, 18, 21], 228.5 cm⁻¹ (E_g) [21], 435.4 cm⁻¹ (E_g) [16], and 620.6 cm⁻¹ (E_g) [16]. These peaks are similar to those reported in the literature, and they are characteristic of the anatase and rutile phases. As in the previous case, it is not possible to observe the presence of the In³⁺ or its oxide phases, and the only apparent difference is a slight shift of the wavenumbers due to a distortion of the lattice structure. In the substitutional case, when In ions take the place of the Ti ions, new bonds O–In–O are formed, which can be active in the Raman spectrum as a bending mode [24]. The lack of contribution from In–O bonds Raman peaks confirms that many In³⁺ ions are introduced in the lattice; therefore, a mismatch in the structure is generated, and it is shown as a shift in the Raman peaks. However, Lan et al. [13] concluded that indium ions might exist as some surface species such as O–In–Cl_x (x = 1 or 2) because the ionic radius of In³⁺ is larger than that of Ti⁴⁺ and there are significant changes in the lattice parameters and cell volume.

On the other hand, some peaks around 302 cm^{-1} and 521 cm^{-1} are present in samples PTI02, PTI03, PTI04, PTICu, and PTIIn; this effect is due to the lack of coating of the TiO_2 structures on the PS, as it was seen in the SEM images. According to the literature, these peaks are characteristics of crystalline silicon. Due to the formation of pores in Si, the peak at 521.5 cm^{-1} must shift to a lower frequency [16]; however, in this case, the higher-frequency shift could be explained by any interaction effect of the TiO_2 with the PS. Also, the peak at 302 cm^{-1} is explained due to the formation of silicon nanocrystal embedded in a PS matrix [16].

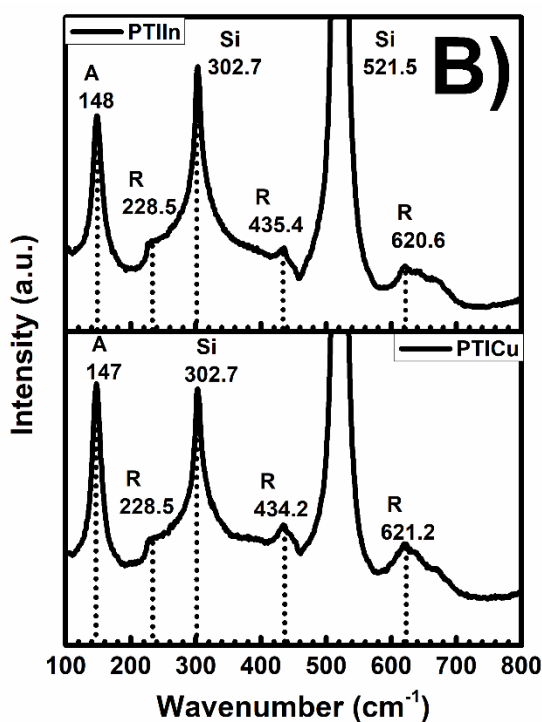


Figure 6. b) Raman spectra of TiO_2/PS structures with Cu and In dopants.

3.3 Optical characterization

Photoluminescence spectra are presented to know the luminescent effect produced before and after depositing TiO_2 structures. Analyzing PL signals is very important to understand the behavior of photons generated by the electron–hole recombination effect. The results are summarized in Figure 7 for PS etching chemically and coating for TiO_2 structures. The PS

shows a broadband, with a maximum emission of around 648 nm or 1.9 eV with a full width at half maximum (FWHM) around 0.5 eV, similar to Leontis et al. [25]. Moreover, it is possible to observe a weak shoulder around 807 nm. In this case, the PL effect could be due to the structure and morphology of the PS, since the porosity can be seen as Si nanocrystals interconnected with different sizes along with the tubular structure [25]. The peak position of the PL depends mainly on the size distribution and chemical composition [25]. In order to explain the origin of the PL in these porous structures, many models have been proposed as quantum confinement [26, 27], hydrogen termination in nanocrystals [28], oxidized nanocrystals [27, 29], localized states [27, 29], and structural defects at the surface [25, 30]. The most accepted model is quantum confinement. This effect takes advantage when the crystalline Si size is comparable with the Bohr radius of excitons in the Si crystals (around 5 nm) [31]. A study performed by Cong et al. [31] mentions that the PL peak at 700 nm is due to the quantum confinement originated by Si nanocrystal coating silicon nanowires. Also, they have a slight emission of around 800 nm, as in this study. This effect attributes to electron–hole recombination confined in Si crystals with a diameter of a few nanometers [31]. The origin of this peak could be corroborated with the Raman spectrum peaks found around 302.5 cm^{-1} , where the peak is explained, due to the formation of silicon nanocrystal embedded in a PS matrix [16, 22].

Sanders and Chang [32] proposed a silicon quantum wires model, where four sub-bands in the conduction band and four sub-bands in the valence band close to each other generate multiple peaks and a band broadening that can be observed through a deconvolution process of the spectrum. By using this model [32], the silicon wires can be treated as one-dimensional structures similarly to quantum-wells, where the energy levels can be represented as

$E_1 \propto 1/L^2$ where L is the size of the well.

Hence, this study proposes that there is a minimum of energy around 8 meV [33] among these sub-bands, which produces an overlay, creating the continuum band effect, as can be observed in the PS spectrum of Figure 7. Also, this effect could originate due to the variation of silicon crystal size; thus, the PL would be a statistical average of the silicon crystal size [33] as it is usually treated for isolated silicon quantum dots [29].

However, it is not possible to discard effects such as oxidized nanocrystals, hydrogen-terminated crystals, or defects at the surface, since due to the preparation method, these three effects are present. A study of FTIR could confirm the first two defects (as is presented in Refs. 34 and 40); meanwhile, defects at the surface have been confirmed by SEM images (see Figure 3a). PL could be a contribution to both defects and quantum effects.

On the other hand, the PS with TiO₂ coating has an interesting effect, as shown in Figure 7. A passivation effect of the PS surface is evident, since the broadband at 648 nm disappears and a new blue shifting band appears. The passivation effect of the PS can corroborate with the TiO₂ coating on the PS surface. The PL for TiO₂ has been explained with three origins: the self-trapping excitons, the oxygen vacancies, and the surface states [34, 35]. However, other studies add another origin from the band-to-band transition [35].

In the literature, the PL of the anatase TiO₂ phase divides into three regions for low energies under 2.65 eV, which is attributed to TiO₂ surface states. Medium energies from 2.7 to 2.84 eV correspond to the recombination of photo-induced electrons and holes via the oxygen vacancies with two trapped electrons. High energies over 3.01 eV near band edge emission are attributed to indirect transitions [35].

In this study, it can be observed these three regions with different intensities that depending on the sample. A green emission has been observed in structure PTI03, which is sometimes reported and is due to a transition of electrons from the donor level of the oxygen vacancies

in the valence band [34]. According to the literature, the oxygen vacancies are intrinsic defects and are created to maintain the charge imbalance [35]. Moreover, they seem to be the most important source in the luminescent emission for TiO₂ denominated V_O, V_O⁺, and V_O⁺⁺ [34]. PL, both PS and TiO₂, structures have been already analyzed, and it is possible to say that TiO₂ PL signal changes depending on both the synthesis conditions and morphology.

Figure 7a shows the spectra of the un-doped samples. Sample PTI01 shows a maximum of PL around 2.61 eV, due to surface states generated by the recombination of photo-induced holes [35]; these surface states can be generated by the large surface area of the nanosheets (see Figure 4a). Sample PTI02 shows a blue shifting related to PTI01, and this could be due to the reduction in titanium butoxide concentration and the morphology change from nanosheets to short nanorods (see Figure 4c), the maximum PL is observed around 2.84 eV due to recombination from oxygen vacancies [35]. However, sample PTI03 shows a redshift around 2.07 and 2.28; in this case, the effect can be explained by a contribution of TiO₂/PS since, as shown in Figure 4e, the TiO₂ does not fully cover the PS surface; for that reason, this luminescent effect can be a contribution of TiO₂/PS interaction. Also, these peaks can be due to oxidized PS, as it is shown in Ref. [36]. This PL contribution could be present in all samples, but the PL intensity could be minimal for the rest of the samples, which avoids the observation of these contributions. However, if this contribution of the oxidized PS or the PS does not exist, the connection between alkoxide concentration and PL energy tends to grow. Also, the tendency can be related to the size of the TiO₂ structure, since as the energy increases the TiO₂ structure reduces; this is only suitable for the samples where titanium butoxide concentration reduces.

On the other hand, sample PTI05 synthesized with acetone shows the maximum PL at 3.04 eV, while sample PTI04 synthesized with methanol shows the maximum peak at 2.9 eV.

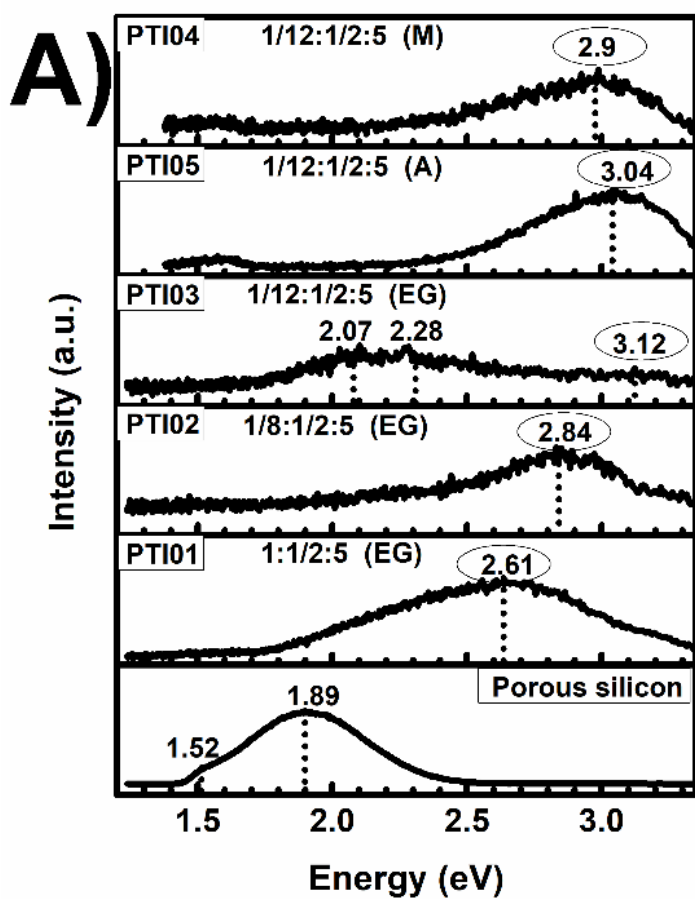
Thus, the change of the solvent produced a redshift in maximum PL energy. If the highest energy for sample PTI03 is considered to be 3.12 eV, it is possible to modulate the emission energy of the TiO₂ structures, both varying the titanium butoxide concentration and changing the solvent.

As it showed the non-doped and doped TiO₂ samples in Figure 7b possess an identical maximum energy intensity, around 2.9 eV, which could be related to a transition from the oxygen 2p level in the valence band to the oxygen defect level [37] and the variation of the energies must be produced for the dopants inserted in the TiO₂ bands. The doped samples have a blue or red shifting. Due to the possible formation of new bonds, such as Ti–O–In, a new In 5p level is introduced above the oxygen 2p level as an acceptor type level [38].

Something similar behavior could occur with the insertion of Cu dopants because of the formation of Ti–O–Cu in response to the charge imbalance which arises when Ti⁴⁺ is replaced by a lower valence ion (Cu²⁺); that is compensated by forming an oxygen vacancy. The most stable site for this compensating of oxygen vacancy is the O site, neighboring the Cu dopant in the equatorial position, which has a computed formation energy of –0.35 eV [39]. Additionally, in all samples, an observable broad PL band could also be associated with optical transitions related to anatase and rutile phases [24].

A second weaker visible band around 800 nm (~1.5eV) could be related to the interaction of the PS layer or be produced due to the rutile phase as Mashary et al. [24] claim (the inset image in Figure 7b shows a zoom-in of the peak). They mention that the rutile phase usually shows PL bands 1.5 and 1.75 eV, which could be related to possible radiative recombination between midgap trapped electrons and free holes at the valence band. It is not clear what the origin of this band is, despite XRD and Raman characterizations show a contribution of the rutile phase in both samples. Another unexpected fact that is worth to mention is the intensity

of the PL spectra, and the PL intensity increases depending on the dopant in comparison with the non-doped TiO₂ sample. This effect might indicate that the formation of new bonds and the insertion of new energy levels (caused by metal dopants). These bonds generate an enhancement in the radiative recombination due to an increase in the free carrier concentration [38] and a suppression of photogenerated electron-hole recombination [14].



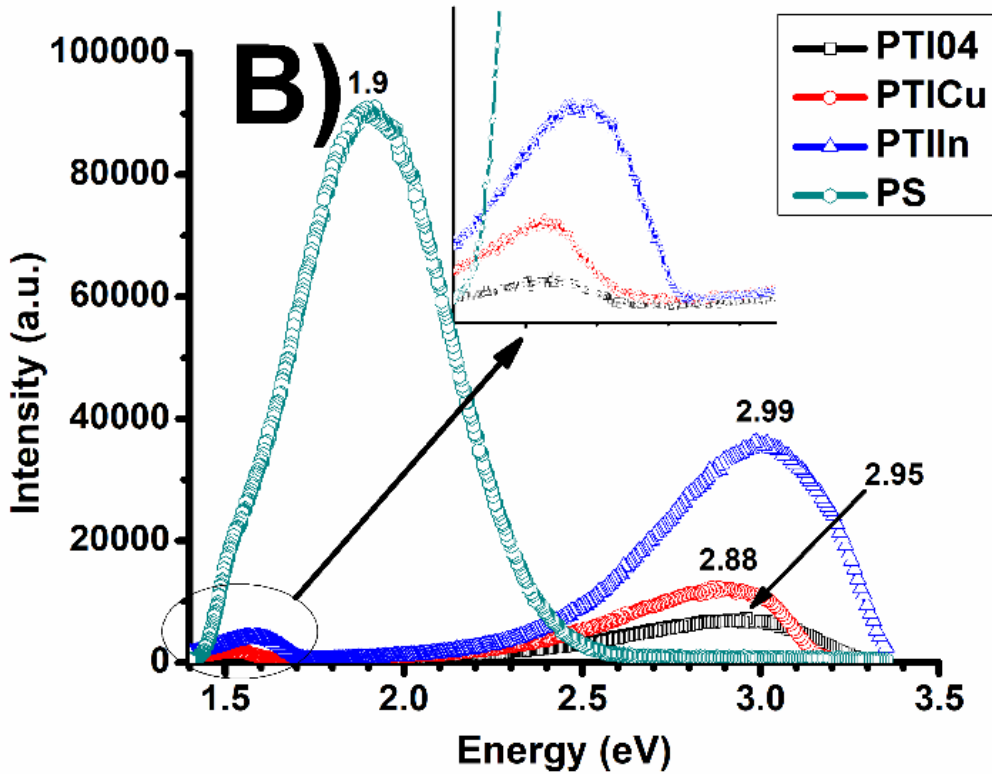


Figure 7. a) PL spectra of the PS and un-doped TiO₂/PS samples b) PL spectra of PS layer and Cu and In-doped TiO₂ heterostructures.

Diffuse reflectance has been used to obtain the energy gap of the samples. By using the Kubelka-Munk method, it is possible to obtain the bandgap of the TiO₂ samples. The equation (eq. 1) for this method is

$$F(R) = (1 - R)^2 / 2R \quad (\text{eq. 1})$$

where R is the reflectance and $F(R)$ becomes the absorbance [12]. Since $F(R)$ represents the absorbance, in Figure 8a, it is clear to see that there are different absorbance bands. To determine the gap, we have extrapolated two lines on the different slopes on the graphs, and the intersection of these lines was the bandgap.

The first absorbance band due to excited electrons from the valence band to the conduction band ranges from 250 to 300 nm, the second band runs from 350 to 400 nm, and the third

band runs from 400 to 700 nm ($2B_{1g}$ to $2E_g$ transition [12]) similar to Choudhury et al. [12]. The literature reports that the valence band is composed of oxygen 2p states, and the conduction band is composed of Ti 3d states [12]. Spectra in Figure 8a are identical among them; we consider that the PS contributes strongly to the absorbance spectra, which means the PS works as an active layer absorbing the UV energy. Therefore, all bands can result from the interaction between PS and TiO₂.

The most important effect is present in samples PTI01 and PTI05, where the effect of TiO₂ is more evident since the contribution of the PS eliminates according to the Raman spectra (where the Si peak contribution does not appear), and the reflectance spectra corroborate with this, showing a significant difference in comparison with the other spectra. For that reason, the real nature of the TiO₂ observes in these two samples because there is no interaction of the PS. Figure 6b–i shows $(F(R)*h)^{1/2}$ versus h to determine the bandgap of the structures. The fractional exponent is due to TiO₂, which is considered an indirect semiconductor [12]. Figure 8b shows the PS energy bandgap around 1.67 eV, similar to what reported in Ref. [40]. Bandgap for TiO₂ structures is presented in Figure 8c–g PTI01, PTI02, PTI03, PTI05, and PTI04, which possess almost the same energy gap, 2.94 eV, 2.95 eV, 2.96 eV, 2.95 eV, and 3.01 eV, respectively. These values around 2.9 eV can be explained with Figure 9 as a result of the insertion of the oxygen level defect close to the conduction band, which causes a direct transition from the valence band edge to the oxygen level defect [37]. This transition makes that TiO₂ structures tend to this kind of transition.

On the other hand, it is possible to observe a tendency for samples PTI01, PTI02, PTI03, and PTI04, i.e., there is an increase in the energy gap as the agglomeration size decreases. Meanwhile, sample PTI05 does not follow the tendency, perhaps due to the structure obtained since, according to SEM images, it seems to be a well-defined 3D structure constituted for

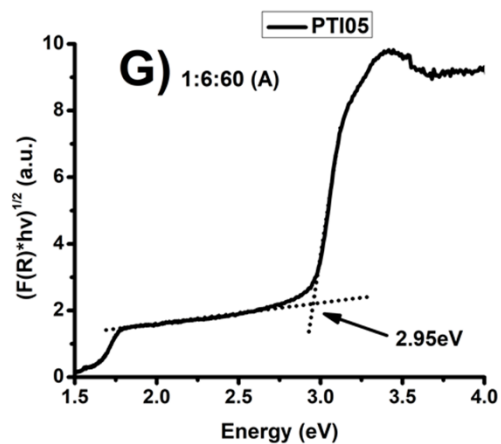
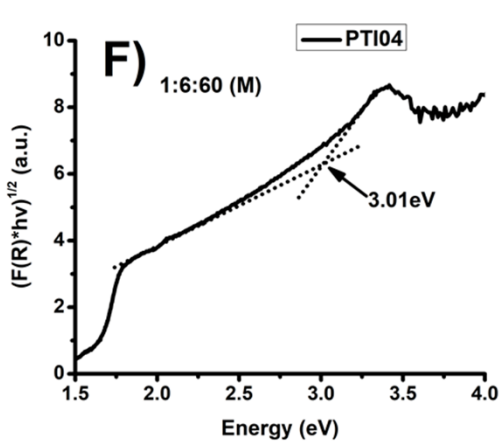
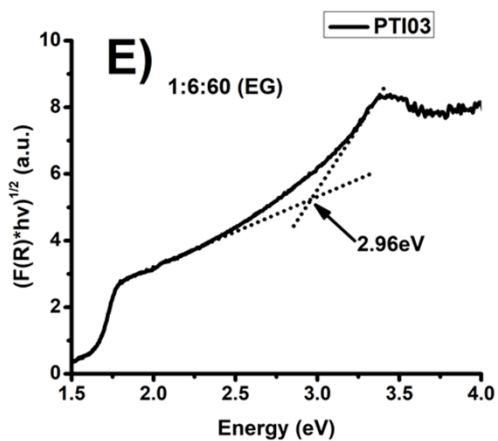
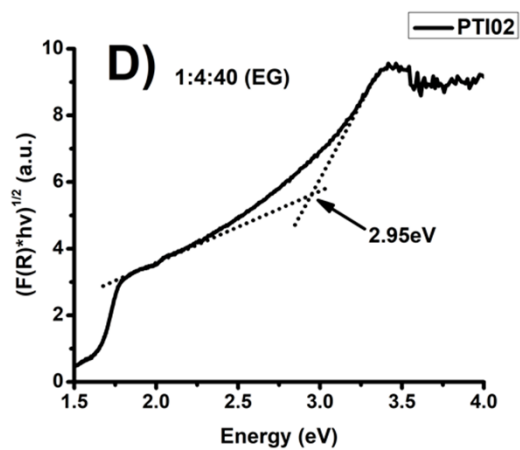
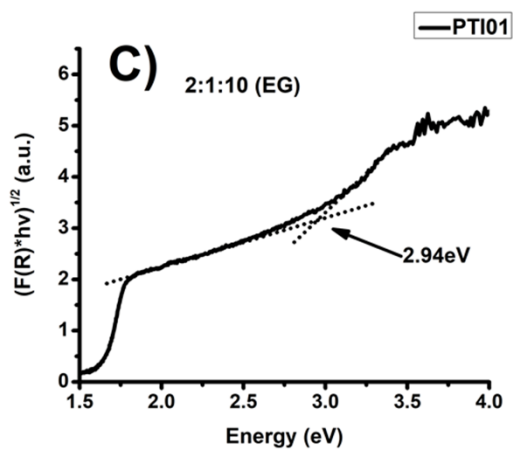
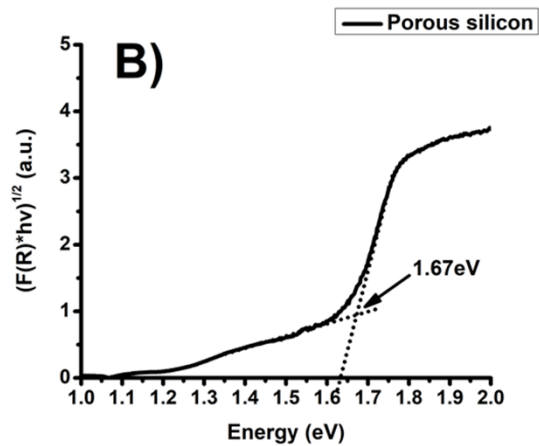
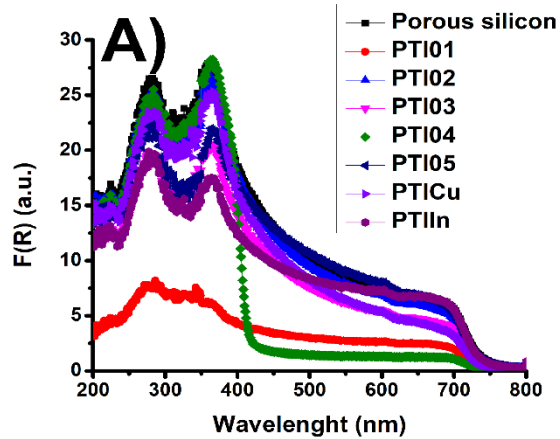
1D structural arrays, in contrast with the other samples that seem to be agglomerations formed from smaller structures. Moreover, the phase change shown in the Raman spectra can be another possible option that explains the discontinuity in the tendency previously found. This effect means that sample PTI05 shows direct band-to-band transitions due to the predominant rutile phase.

The PTICu sample (Figure 8h) has a bandgap around 2.95 eV that can be attributed to the insertion of the Cu^{2+} dopants and oxygen defects, which form sub-bands states in the TiO_2 bandgap. Thus, in the Cu-doped TiO_2 , the electrons can be excited to make a direct transition or to occupy Cu^{2+} s-d states, and the oxygen vacancies capture electrons [12]. The oxygen vacancy states such as F^+ (single electron) and F^{++} (devoid electron) are responsible for the capture of electrons. Therefore, the sub-band states of Cu^{2+} and oxygen defects are responsible for the reduction of the bandgap of TiO_2 [12].

The PTIIn sample (Figure 8i) has a bandgap around 2.92 eV that can be related to the introduction of the In 5p level or to an oxygen level defect, as previously mentioned. The reduction of the bandgap for doped samples indicates the insertion of different levels inside of the TiO_2 bandgap. Moreover, the bandgap reduction can be controlled by the surface of the nanostructures, lattice strain, and vacancies [12].

On the other hand, it is possible to determine the width of the defect bands in the TiO_2 (samples with Cu and In) bandgap employing the Urbach energy (E_u). This energy is related to the Urbach tail, which refers to the creation of a band tail due to defect states, which extends far down the bandgap from the lower part of the conduction band, and similarly, the defect states near the valence band localized in edge deep inside the gap [12]. The reciprocal of the slopes of the linear portion, below the optical bandgap, gives the value of E_u [12]. The Urbach energies are 69.5 meV and 83.2 meV, for PTICu, and PTIIn, respectively. The

bandgap of samples with Cu and In is 2.95 and 2.92 eV, respectively. Therefore, the gap reduces in these two samples, but the magnitude of defect energy increases, similarly reported by Choudhury et al. [12]. Choudhury et al. argument that the formation of sub-band states between valence and conduction bands result in the narrowing of the band gap.



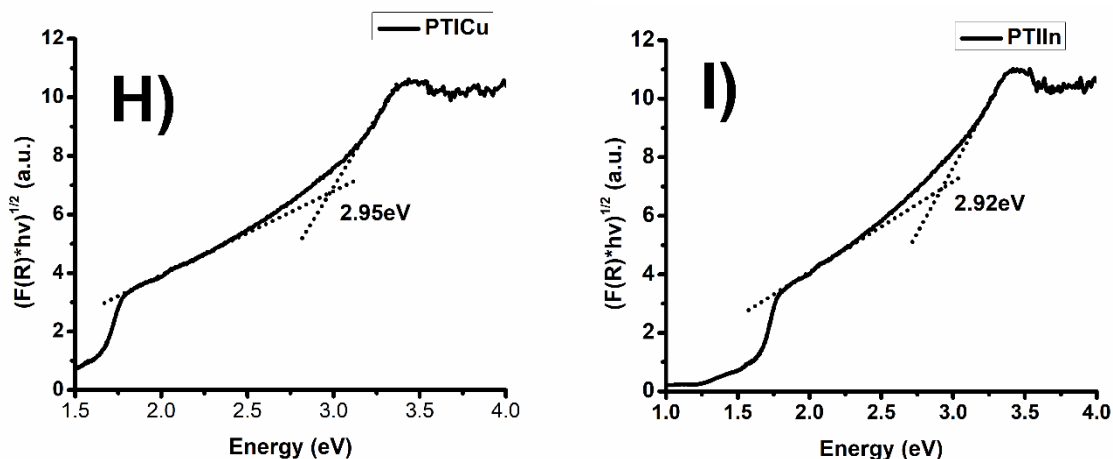


Figure 8. Diffuse reflectance of the TiO₂ structures and Kubelka–Munk method to determine the bandgap: a) Kubelka–Munk absorption, b) determination of E_g for PS, c) determination of E_g for PTI01, d) determination of E_g for PTI02, e) determination of E_g for PTI03, f) determination of E_g for PTI04, g) determination of E_g for PTI05, h) determination of E_g for PTICu i) determination of E_g for PTIn.

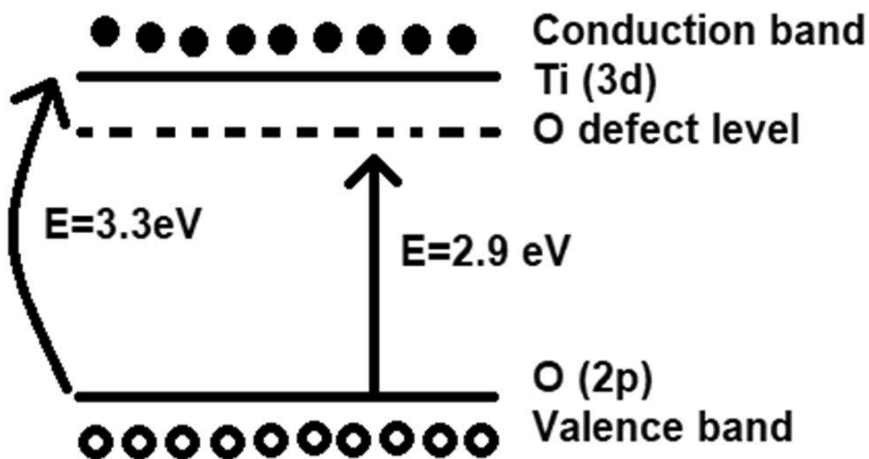


Figure 9. Energy band diagram of TiO₂ showing the transition from the valence band to oxygen defect level.

3.4 Application as oscillator

Oscillators are basic blocks in most of the electronic systems. They often generate sinusoidal or square waveforms. Therefore, they are widely used in different applications, such as clock signals that regulate computers and synchronize signals. Among the several types, relaxation oscillators are built using reactive elements (i. e. capacitors) which consume large area especially in the low frequency applications. [41] A simple relaxation oscillator is designed by directly coupling a RC timing network to a passive S-shaped current-controlled nonlinear device [42].

To understand the contribution of porous silicon to the TiO₂/PS heterostructures, it was analyzed before the deposition of TiO₂. In order to understand the structure and electronic transport in macroporous Si on bulk Si.

For that reason, electrical contacts were deposited to characterize the electrical properties of the PS/c-Si heterojunction in the same way as the whole heterostructures with TiO₂. From the I-V characteristics shown in Figure 10a, it can be seen that the transport is asymmetric with respect to polarization, with small activation energy of 70 meV for reverse polarization. However, the structure conducts electricity in both polarizations, in contrast to a typical rectifying diode. This behavior has been reported for mesoporous Si/c-Si heterojunctions, with defects cured by an H₂ treatment [43].

In the present case, the amount of defects is not as high as in mesoporous Si produced electrochemically (sponge-like); these defects do not represent traps, but decrease the number of available carriers in comparison to c-Si, producing the small barrier for reverse polarization. Figure 10b shows the energy band diagram of the heterojunction. The bandgap of PS has been considered 1.67 eV, as the optical bandgap is estimated in the previous work

[44]. This value is close to the value of about 1.8 eV reported for electrochemically prepared PS with identical porosity [45, 46]. Due to the lower availability of charges in PS, this material is considered p^- , as compared to the substrate, which is p . It has been reported that the semiconductor type does not modify when there are pores. However, the conductivity of the material is reduced when the porosity increase. The carriers that are available to conduct are the ones that are originally available on the p -type silicon wafer. Surface defects introduced by etching the semiconductor only partially contribute to the conductivity [47, 48]. On the other hand, it is essential to clarify that the traps produced by metals are clearly electronically driven; however, surface defects can donate holes or electrons depending on the surface chemistry.

It is important to mention that the junction's energy barrier does not represent an important practical impediment for electrical transport since it is not much higher than the thermal energy at room temperature (about 26 meV).

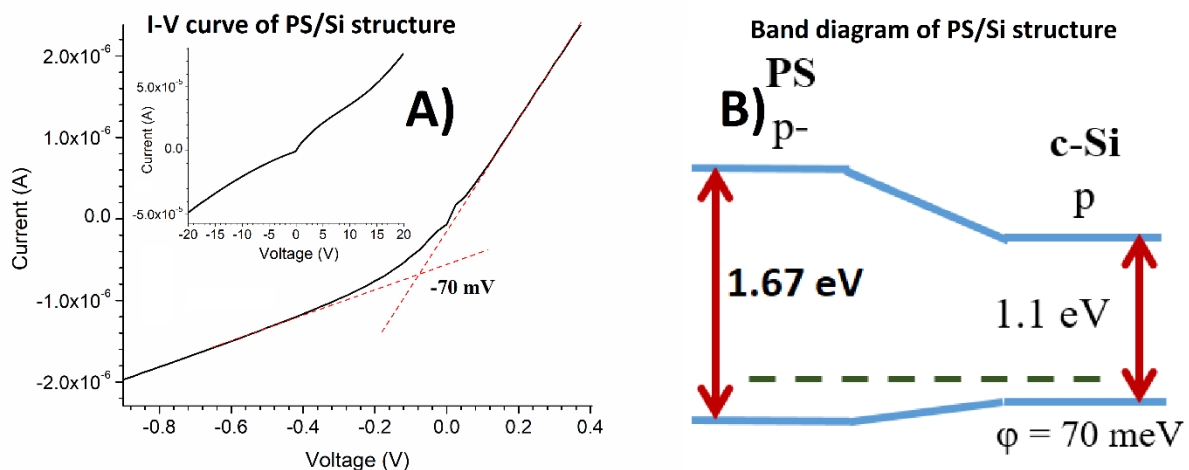


Figure 10. a) I-V characteristics of the PS/Si structure b) Energy band diagram of the PS/Si structure.

As it has been seen, there is no problem for the junction between porous silicon and bulk silicon. So, will be analyzed the structure and electronic transport in TiO₂/macroporous Si heterostructures (tunnel diode-like behavior).

Figure 12 shows the electrical characterization of the TiO₂/PS heterostructures under darkness and illumination conditions. The heterostructures were measured from negative to positive voltages and limiting the current to 10 mA to avoid any damage to the heterostructures. Figures 12a, 12b, 12c, 12d, 12e, 12g, and 12h show the current-voltages characteristics. For negative voltages, the heterostructures present different compartment. For example, the sample PTI01, PTICu, and PTIIn (Figures 12 a, g, and h) show a linear region, which is characteristic of resistive conduct that could be associated with the high resistivity of the TiO₂ morphology or the PS layer. The samples PTI02 and the PTI04 (Figure 12b and 12d) show a quasi-resistive behavior.

Meanwhile, PTI03 and PTI05 samples (Figures 12c and 12e) display a rectifying tendency. As can be observed, the shape of the curves is very equal to the I-V characteristics of tunnel diodes [49]. This behavior confirms that the TiO₂ layer is responsible for the free or not-free transition of injected electrons through the nickel contact. I-V curve of isolated porous silicon corroborates this affirmation, see Figure 12f.

On the other hand, interesting effects were found for positive voltages, which is characteristic of the I-V curves of tunnel diodes, this characteristic is a section of negative differential resistance (NDR). This effect has already been reported, [50, 51]. An abrupt current reduction characterizes this effect as the voltage increases. This effect appears in the all samples, except for the PTI05 (Acetone) Figure 12f corroborates that the TiO₂ layer causes this effect since the porous silicon I-V curve does not present it. The reduction of the current starts from 3 to

6 V approximately, which depends on the sample. The NDR effect has been widely studied to try to explain its origin. Models such as tunneling, Coulomb blockade, and charge storage have been suggested as the leading causes for this effect [50].

In the literature, the NDR effect has been observed in different materials such as TiO₂ [52], graphene [53], arsenene [54], silicon-rich oxide [55], and others [56, 57]. Moreover, many models proposed trying to explain this phenomenon, such as resonant tunneling, Coulomb blockade, charge storage [50], structural asymmetry [53], vacant defects [54], non-equilibrium carrier density excess [57], Van Hove singularities [58]. This NDR effect was observed for the first time in 1958 [49]. However, depending on the heterostructure, this effect can be explained by some models. In our case, it has been analyzed each model to find the most exact one for the behavior of our heterostructures. In the resonant tunneling, the NDR effect occurs when quantized states can no longer assist the coherent tunneling through the double-barrier structure [58]. The Coulomb blockade model is observed in a simple system where the electrons can tunnel to the dot by applying a voltage to the gate electrode (which is capacitively coupled to the dot). If one electron tunnels to the dot, the electrostatic energy (Coulomb charging) is increased as:

$$\Delta U = q^2/2C_{dot} \quad [59] \quad (eq. 2)$$

When the dot is sufficiently small (C_{dot} is small) and ΔU exceeds the thermal energy, even a single electron cannot tunnel to the dot without the help of external gate bias to overcome the Coulomb repulsion of the dot. This effect is called the Coulomb blockade [59]. Marin et al. [50] mention that the Coulomb repulsion is caused when the conduction channels are blockage due to carrier trapping phenomena in the SiO₂/Si interface.

Charge storage model is proposed for MIM structures. In that case, the silicon monoxide layer sandwiched between two electrodes. Electron-trapping states are generated in the insulator layer. These trapping sites create charge storage, which reduces the current through the junction. Moreover, the interface layer close to molecular dimensions causes the NDR effect, and the charge storage is a result of a resistive switching model based on charge trapping and de-trapping at a bandgap state introduced by oxygen vacancies, with molecular oxygen ions [60]. The structural asymmetry is originated from the asymmetric distribution of the transmission spectrum concerning the Fermi level. The localization of the LDOS explains this asymmetric in structures based on carbon [61]. Vacant defects not only are related to the charge storage but also the localized defects and the structure of the morphology. In this case, the NDR effect could be observed in the armchair structure of nanoribbons [54]. Van Hove singularities are related to the electrodes. In this case, the metal electrode has to be a transition metal, and the electrode must have a Van Hove singularity in its density of states. Moreover, this will occur if the contact electrode is in 1D, and if semiconductor has parabolic bands [58, 62].

All these models that try to explain this NDR effect could be accepted, but as could be seen, the material is important. Therefore, in a report of a tunnel diode, TiO_2 has been used just as a physical nanometric barrier (deposited by ALD) [52]. In the present case, the tunneling barrier is formed by the TiO_2/PS junction. To be able to explain the tunneling process, it is simpler considering the band diagrams of the heterojunction (see Figure 11). For simplicity, the $\text{PS}/\text{c-Si}$ junction is not shown in the band diagrams because this junction does not limit carrier transport as it is seen in Figure 10. Under conditions close to an open circuit and when applying small positive voltages (reverse polarization), the observed current is given by

minority carriers (indicated with thin arrows in the diagram of Figure 11a). As can be observed, the bands bend to reach equilibrium, producing a large barrier of about 1.2 eV for electrons, the majority carriers. TiO₂ is commonly an n-type semiconductor [37, 63], with a bandgap of 3.3 eV. The donor level is about 0.4 eV below the conduction band and is given by defects related to oxygen-sites [37]. When direct polarizing (negative voltages, as in Figure 11b above the potential barrier, the negative current increases steeply. The thick arrow indicates the current of majority carriers. On the other hand, when we reverse polarizing at potentials much larger than the bandgap of PS, the electrons can tunnel through the barriers ballistically (see Figure 11c), competing with the current of minority carriers. The tunneling current is not high because the materials are not highly doped, and consequently, the barrier is not so narrow; however, it is high enough to compete and cause a decrease of the overall current, producing NDR.

PS/TiO₂ band diagram.

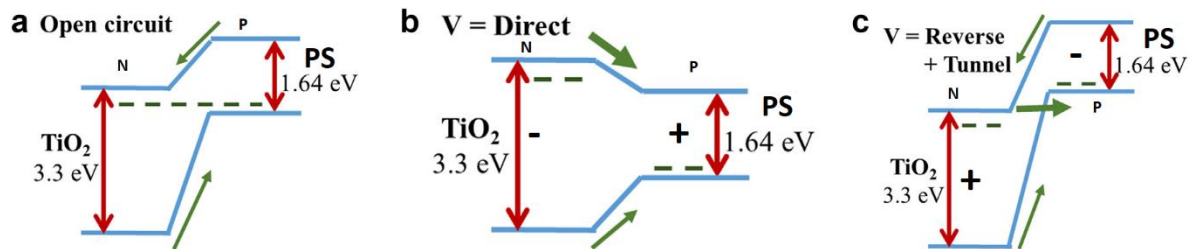
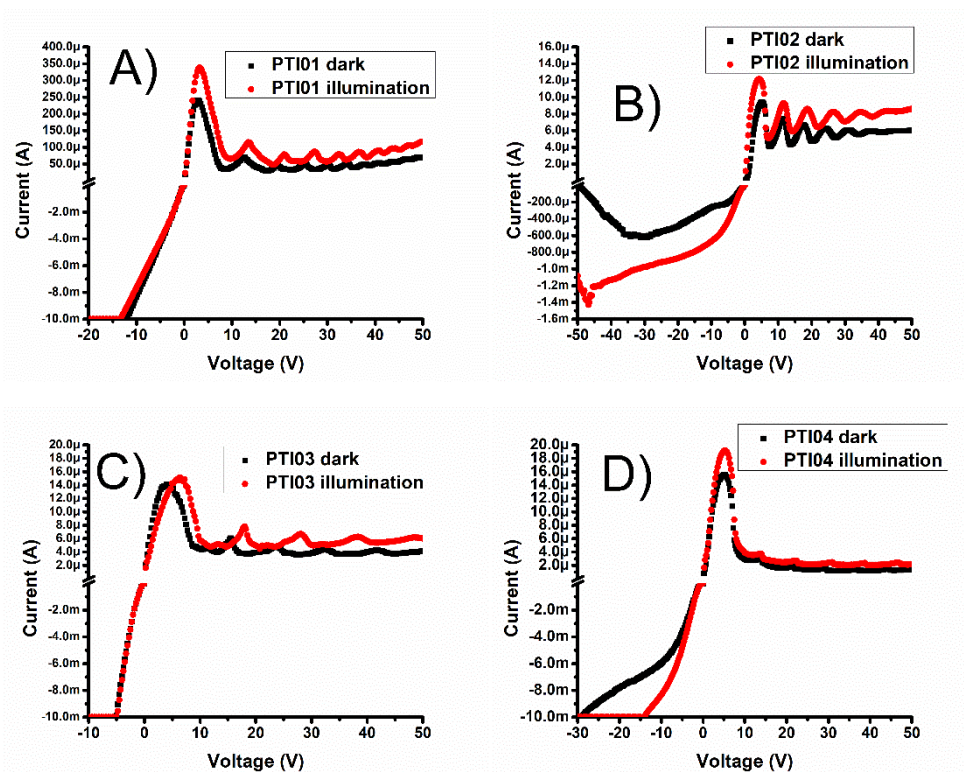


Figure 11. Band diagrams of the TiO₂/PS heterostructures under different external voltages: a) close to open circuit conditions, b) direct polarization, at voltages larger than the energy barrier for electrons, and c) reverse polarization at the voltage of tunneling effect. The thick arrows represent currents of majority carriers, while the thin arrows represent currents of minority carriers.

On the other hand, we could find a tendency concerning the bandgap vs voltage where the current decreases. The samples PTI01, PTI02, and PTI03 show a shifting for the NDR voltage (the voltage peak where the current starts to decrease and those are 3.4, 4.3, and 6.3 V, for PTI01, PTI02, and PTI03, respectively) as well in the bandgap. It means the voltage peak

increases similarly as the bandgap does it (2.94 eV, 2.95 eV, 2.96 eV for PTI01, PTI02, and PTI03, respectively). Thus, the optical (bandgap) and the electrical properties are related to the morphology and size of TiO₂ particles. This voltage shifting could be due to the specific surface area (related to morphology) or the distribution of the TiO₂. The electrons are easily transported through the heterostructure when the morphology is a nanosheet (sample PTI01). The sample PTI02 presents nanospheres with short nanorods, which creates more resistance for the electrons flow. The sample PTI03 presents nanoparticles with different sizes; this distribution of size generates a wide bandgap, as in the case of Si nanoparticles. Thus, the conduction proceeds via complicated paths in search of the same size particles, resulting in longer paths, hence lower mobility [64]. For the rest of the samples do not find a tendency.



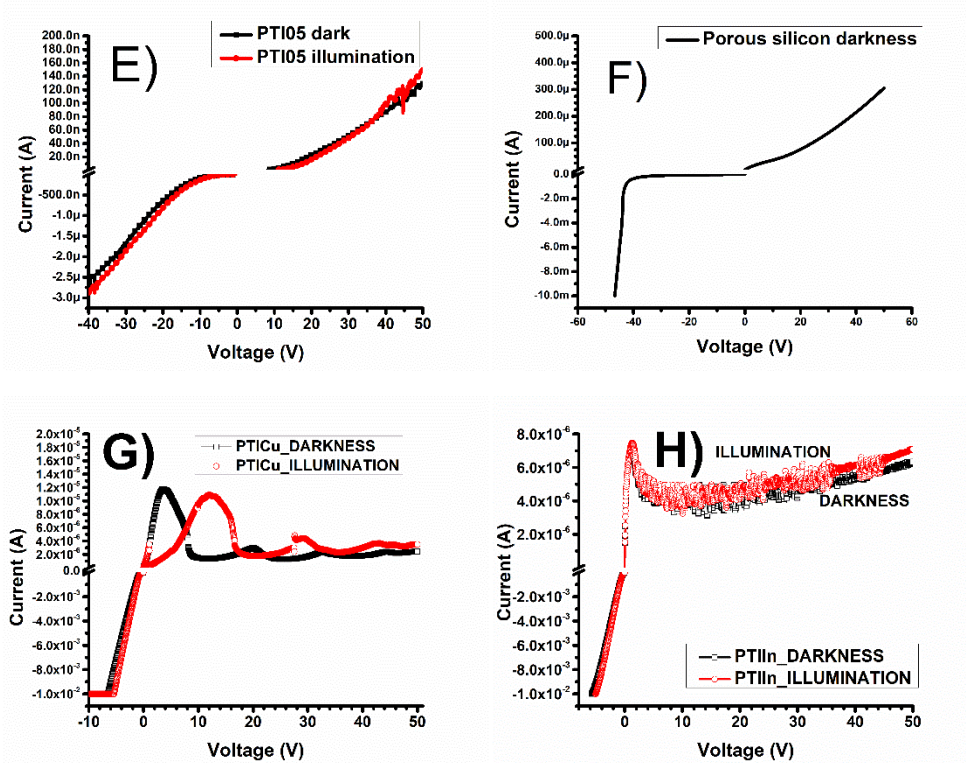


Figure 12. Electrical characteristics of the TiO₂/PS structures a) PTI01 b) PTI02 c) PTI03 d) PTI04 e) PTI05 f) porous silicon, g) PTICu, and h) PTIIIn.

Moreover, as could be observed in figure 12, the most of the heterostructures showed oscillations. In insets of figure 14 can observe the oscillations fully periodic. Figure 13a shows a representation of a couple of TiO₂ particles attached to a pore wall, together with an electrical model of the system's physical elements. As evidenced by the I-V curves, the TiO₂/PS interface represents a junction that can be modeled with a rectifying diode. On the other hand, the dielectric characteristics of the TiO₂ particles give rise to a capacitance. That capacitance should be charged and discharged during the recording of the I-V curves, as indicated the Figure 13b. An important fact of capacitors is that they store charges, and the local voltage depends on the amount of stored charge.

Furthermore, the diode's voltage is the same as the one of the capacitor, since they are connected in parallel (see Figure 13a). As soon as the diode is in the tunneling mode (the capacitor reaches the voltage for the tunneling effect) and the current starts flowing in the opposite direction, the capacitor starts to discharge, and this produces that the local voltage decreases, causing that the diode is not in the tunneling mode anymore. When the diode is not in the tunneling mode, the capacitor charges again, until reaching the tunneling voltage. This process repeats undefined number of times, and it is observable as the temporal oscillations of Figure 14. The complete simplified electrical model for the whole system, including the external voltage source, is depicted in Figure 13c. Such a circuit (with the effect previously described) is known as “relaxation oscillator”, if the diode presents a trigger voltage (as is the case of tunnel and zener diodes, vacuum bulbs, and neon lamps) [65, 66]. The TiO₂/PS heterostructure investigated in this work may be the simplest relaxation oscillator ever reported, and it is the first report of using TiO₂ or TiO₂ with Si.

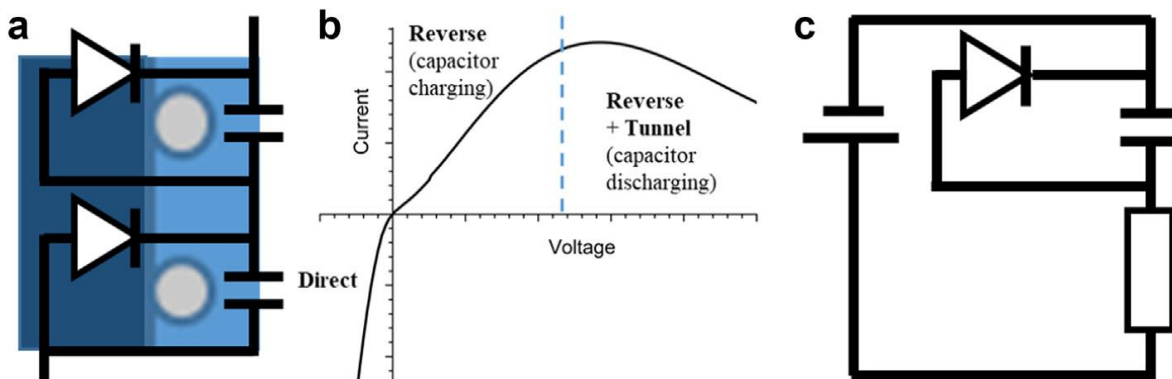


Figure 13. a) Schematic of the interface between TiO₂ particles (circles) and Si pore walls, with their corresponding electrical model. b) Typical I-V curve of the TiO₂/PS heterostructures, indicating the charging/discharging of the capacitors of a). c) Simplified electrical model of the complete TiO₂/PS devices, with external voltage source.

For that reason, the NDR and the oscillations could be explained by the charge storage model [60], and Van Hove singularities [62], since the composition of the heterostructures is similar

to this work. However, the behavior of the PTIn sample could be associated with a Coulomb blockade, which has been associated with telegraph noise produced by trapping and de-trapping of carriers in trap states caused by the SiO₂/Si interface and the diameter variation of silicon nanowires [50] since it is well-known that crystalline Si is oxidized rapidly in environmental conditions and the formation of PS layers generate the silicon nanowires with different diameters.

Moreover, as mentioned above in the diffuse reflectance spectra analysis, the reduction of the bandgap is the result of the introduction of new energy levels (trap states) in the TiO₂ bandgap, and thus, there is a high possibility of the NDR phenomenon taking advantage from the Coulomb blockade model.

In order to get more information of the oscillations, we realized the current-time curves shown in Figure 14. In this case, we polarized the heterostructure with 5 V. The oscillations have never been reported as we show it. Yu et al. [55] reported aperiodic oscillations; however, these oscillations look like kind of noise. They mention that the current bump is produced by static transport of carriers through the silicon-rich oxide (SRO) layer in a specific voltage range.

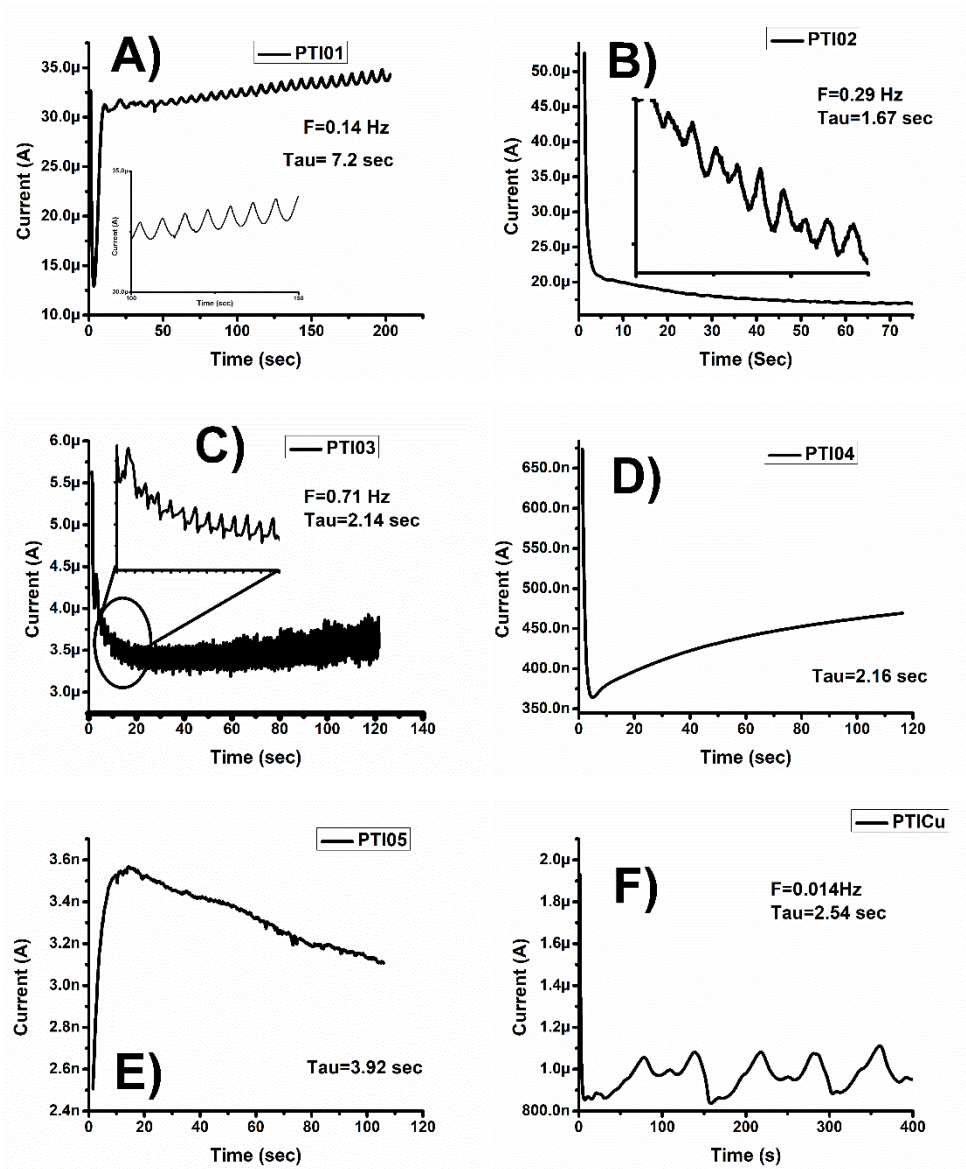
Furthermore, the current oscillations depend on the step delay time. In our case, this effect is completely different because the oscillations shown look like a periodic function. Applying the circuit theory for an RC circuit charge and discharge for a capacitor we obtain the relaxation time

$$0.37 I_0, \text{ where } I_0 = \mathcal{E}/R, \mathcal{E} \text{ is the electric field and } R \text{ is resistance} \quad (\text{eq. 3})$$

Figure 14 shows the current-time (I-t) curves, where we find a relaxation time and the oscillation frequency for some samples. PTI01 has a frequency of around 0.14 Hz, and the

relaxation time is 7.2 sec. PTI02 shows a frequency of 0.29 Hz and a relaxation time of 1.67 sec. The PTI03 sample displays 0.71 Hz of frequency and 2.14 sec of relaxation time. PTICu shows 0.014Hz of frequency and 2.54 sec of relaxation time. PTIIn presents 0.1Hz of frequency and 5.05 sec of relaxation time. We used Fast Fourier Transform (FFT), and we had 0.14 Hz, 0.33Hz, 0.70 Hz, 0.014Hz, and 0.1 Hz respectively, this corroborates the frequency values obtained by the conventional method of an inverse period of time. The oscillations in these sample are periodic as can be observed in the inset as well as the FFT corroborates the frequency. These values of frequency are related to the TiO₂ size. That is, the reduction of the TiO₂ nanostructures generates an increase in the oscillation frequency, which is directly correlated to the energy, as we showed in the bandgap energies and the NDR voltage. Finally, the methanol and acetone samples does not show an oscillation frequency, but the relaxation times are 2.16 and 3.92 seconds, respectively. The samples PTI01 and PTI05 do not show a relaxation time (discharge time); instead of that, we calculate the charge time following equation 3. We use the RC model because Janene et al. [67] reported a similar heterostructure, and they made impedance spectroscopy, and the heterostructure was evaluated applying an electric model based on resistances and capacitors. With this information it is unclear the origin of these oscillations (in the next section will be explained); we believe that could be a result of charge and discharge due to the depletion region formed between the Ni contact and the TiO₂/PS interface. After injecting electrons, there are recombination processes, which charges negatively the TiO₂/PS interface, and the Ni contact positively. Therefore, this effect could be inverted when the charge storage takes advantage of the TiO₂/PS interface, which means, now the TiO₂/PS interface is saturated with a negative charge. Thus, now the interface injects the electrons, the nickel contact is negatively charged, and the TiO₂/PS is positively charged. This charge and discharge produce

the oscillation effect in our structures. For that reason, this new effect can be considered as a relaxation oscillator. Thus, this simple heterostructure is the simplest relaxation oscillator ever fabricated, and it has been done by using straightforward methods.



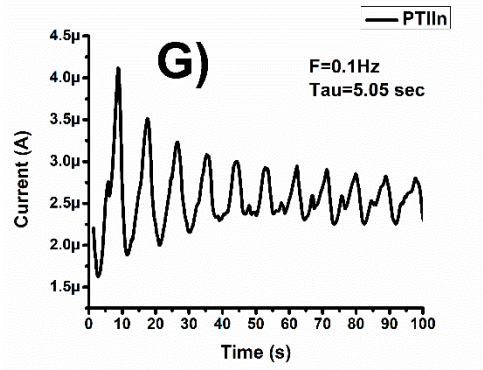
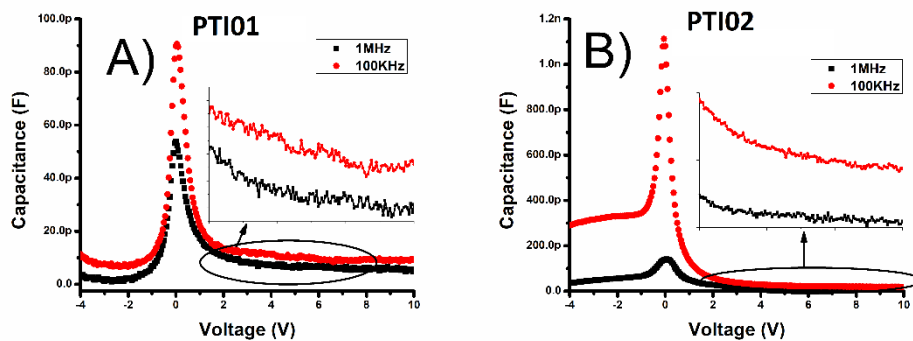


Figure 14. Current-time curves a) PTI01 b) PTI02 c) PTI03 d) PTI04 e) PTI05 f) PTICu g) PTIIIn

To get more information about the oscillations, we carried out capacitance-voltage measurements; Figure 15 shows these curves. We can observe an increase in the capacitance as the voltage increases (negative voltages) until reaching a maximum close to zero, and then the capacitance decreases in an un-exponential way up to become almost constant (positive voltages). This behavior is attributed to the increase in the depletion region, that is, an increase in the built-in voltage [68]. The maximum peaks are characteristics for the inversion region, and the constant capacitance is the depletion and accumulation regions [69]. This behavior is equal to reported in the literature with heterostructures based on TiO_2 [69-72]. In some samples can be observed anomalous peaks or shoulders (Figures 15b, 15c, and 15d) that are equivalent in other reports [69, 71, and 72]. The maximum peak found could be attributed to the density distribution of interface traps/states [72] in our case due to the interface $\text{TiO}_2/\text{PS}/\text{c-Si}$. The shoulder or the second peak is attributed to the series resistance of the heterostructure [71 and 72]. Figure 7a does not show any defect; this means that the series resistance is small, which can be ignored. Also, according to the measurements for two frequencies, we observed a reduction of the capacitance values as the frequency increases, even there is a slightly shifting towards higher positive voltages. These effects have been

explained due to reordering and restructuring of the surface states under electric field [72] or interface states [71]. Interface or surface states at low frequencies can follow the AC signal resulting in an additional capacitance that depends on the frequency. At high frequencies, these states cannot follow the AC signal, and there is not a capacitance contribution. Another explanation for this effect is due to the charge storage owing to the decrease of the dielectric constant [72]. For our investigation, this last explanation could be the most likely because we have the NDR and the oscillations, which is caused by the charge storage effect in the TiO₂ layer. For that reason, we corroborated that this effect is attributed to the charge storage. On the other hand, the inset in Figure 15 displays discontinuities equal to non-periodic oscillations. This effect is presented in positive voltages from Figures 15b to 15d, and Figure 15a is observed in the entire voltage range. These non-periodic oscillations can be attributed to discontinuities in the quasi-1D of the nanowires in the porous silicon layer [73]. Biswajit [73] mention that this phenomenon could be due to large size distribution, and the high resistive layer of PS; however, he suggested that quantum confining structures in PS is most likely, as could be deduced from our previous work [44], where Raman spectroscopy helped to evidence the presence of silicon nanocrystals in PS.



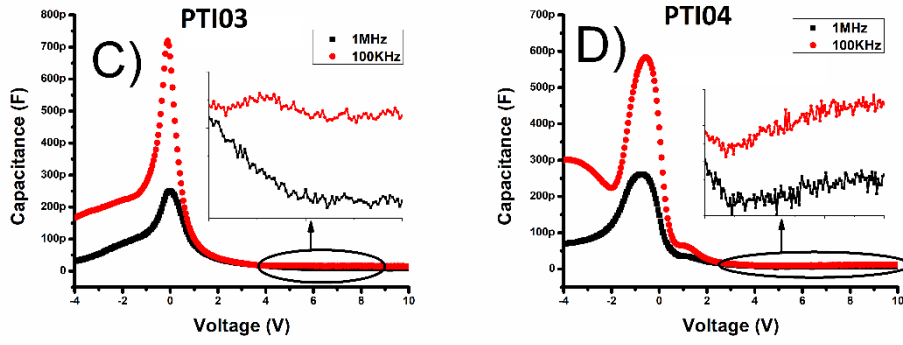


Figure 15. Capacitance-voltage curve a) PTI01 b) PTI02 c) PTI03 d) PTI04.

Figure 16 shows the Mott-Schottky plots of the samples showing good linear behavior in a wide range of reverse bias. In this case, when a positive voltage is applied to the TiO_2 which is considered as an n-type semiconductor concerning the p region (p-type silicon substrate), we can obtain different parameters following the relation between capacitance and voltage as a simple p-n junction capacitor

$$C^{-2} = (2/q\epsilon_s\epsilon_0NdA^2)(V_{bi} - V_r) \quad [72] \quad (\text{eq. 4})$$

Where q is the electron charge, ϵ_s and ϵ_0 are dielectric permittivity of semiconductor and vacuum, N_d is the donor concentration, A is the contact area, V_{bi} is the built-in barrier, and V_R is the reverse bias voltages. From the Mott-Schottky curves, we can obtain the V_{bi} parameter easily because this is obtained by x-intercept extrapolation of the C^{-2} - V graphs.

The diffusion potential can be obtained from

$$V_d = V_{bi} + kT/q \quad \text{where } k \text{ is the Boltzman constant and } T \text{ temperature [69]} \quad (\text{eq. 5})$$

The donor concentration can be obtained from the slope of equation 4 in the Mott-Schottky curves. The equation resulting is

$$Nd = 2/q\epsilon_s\epsilon_0A^2m \quad m \text{ is the slope in the curves} \quad (\text{eq. 6})$$

The depletion layer width was obtained by using the next equation

$$Wd = (2\epsilon_s\epsilon_0Vd/qNd)^{0.5} \quad [72] \quad (eq. 7)$$

The values obtained are tabulated in table 2 for different samples at different frequencies. All obtained parameters are affected by the frequency variation, which could be due to surface or interface states in the heterostructure. In the table 2, it can observe that the diffusion voltage, built-in voltage, and the width parameters follow a tendency inversely proportional the morphology size of the samples PTI01, PTI02, and PTI03 at 100 kHz. For 1 MHz, the samples do not show a tendency. As well for the sample PTI04, there is not a tendency with the other samples due to the solvent change. On the other hand, it is important to mention that the positive slope in the Mott-Schottky curves indicates that the TiO₂ structures are n-type semiconductors [69]. Moreover, the linear region demonstrates that the junction in our heterostructures is abrupt.

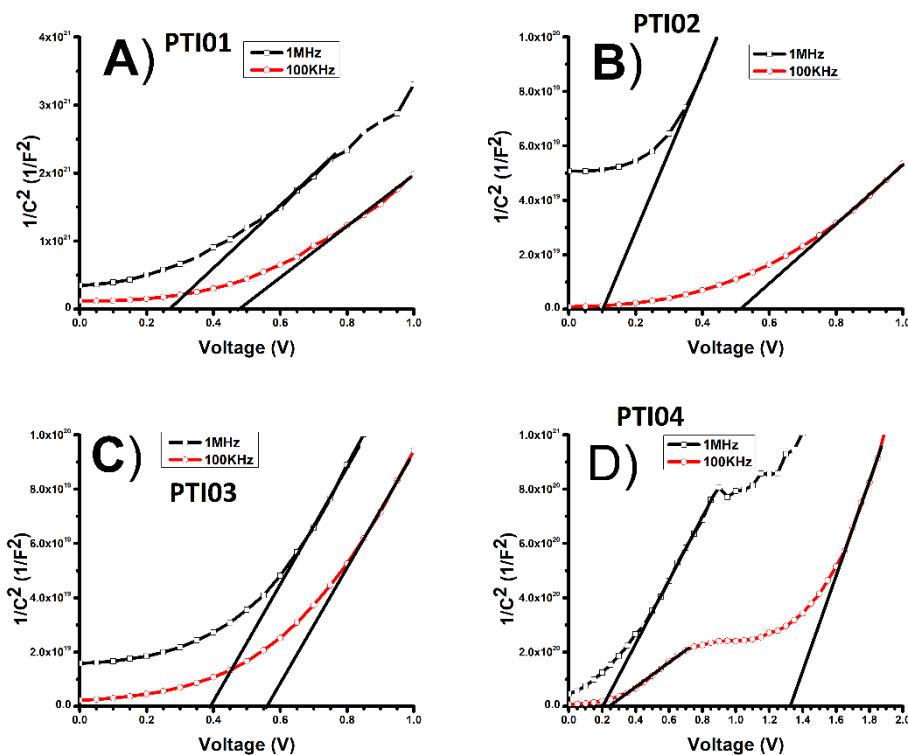


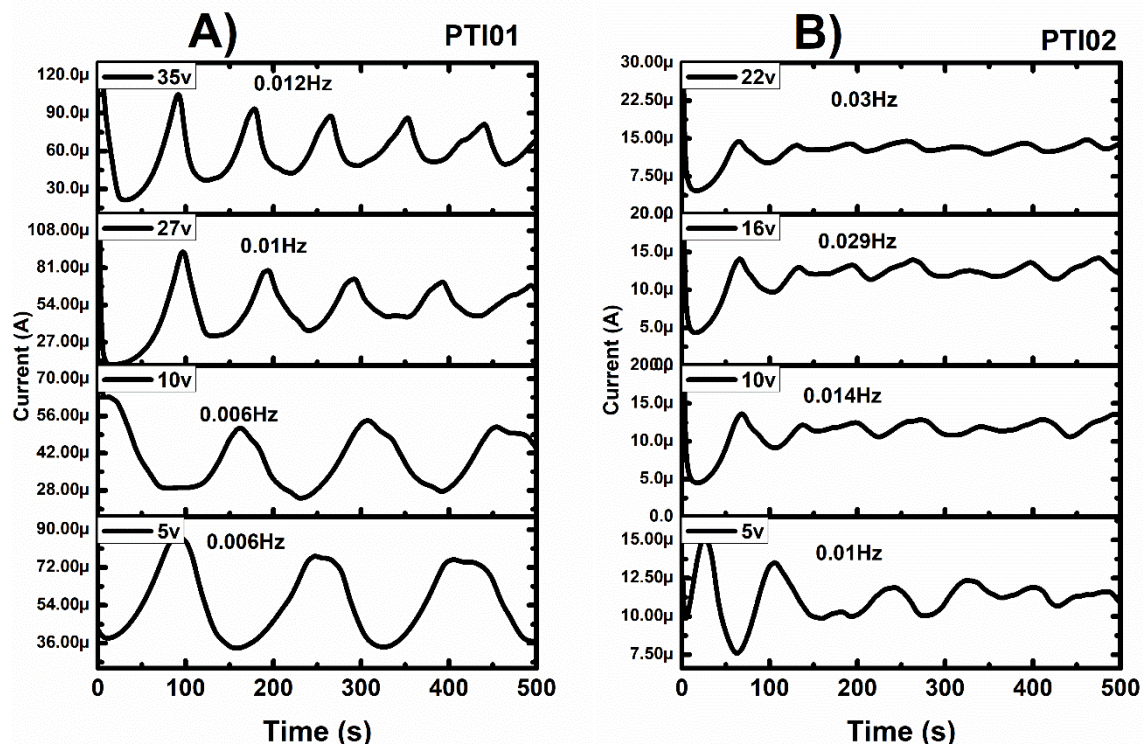
Figure 16. Mott-Schottky plots for a) PTI01 b) PTI02 c) PTI03 d) PTI04

Table 2. Electrical parameters of the TiO₂/PS/c-Si heterostructures at different frequencies

PARAMETER	f	V_d	N_d	V_{bi}	W_d
SAMPLE		(V)	($\times 10^{14} \text{cm}^{-3}$)	(v)	($\times 10^{-4} \text{cm}$)
High-glycol	100KHz	0.5	5.1	0.48	2.9
	1MHz	0.29	3.8	0.27	2.5
Medium-glycol	100KHz	0.53	160	0.51	54
	1MHz	0.12	73	0.1	38
Low-glycol	100KHz	0.57	83	0.55	77
	1MHz	0.41	76	0.39	69
Low-methanol	100KHz	0.27	36	0.25	81
	1MHz	0.21	16	0.19	1.07

As could be observed in I-V curves, the oscillation period changes with time, and its intensity suffers damping. The parameter that changes with the time is the voltage; for that reason, in this investigation we performed different I-t measurements applying different voltages. In these new graphics the frequencies changed for the first three samples (PTI01, PTI02, and PTI03). However, the tendency of the frequency is preserved. Figures 17a to e show the graphics of the current-time curves with different voltages that depended from I-V curves (Figure 12) and previous work where the oscillations occurred. This variation can be explained considering that the morphology of the TiO₂ particles is defect-rich (flake-like shape). In such a case, the exponential factor of the conductivity depends not only on the activation energy and temperature but also on the electric field (i.e., on the applied voltage) [74]. According to this, varying the applied voltage may vary the tunneling voltage and current densities in all samples; thus, its oscillation frequency varies with voltage.

Something else that is worthy to mention is that the I-t curves do not show a remarkable increase of the amplitude despite an increment in voltage (only the PTICu shows an offset). This demonstrates that we can use different voltages affecting only the frequency.



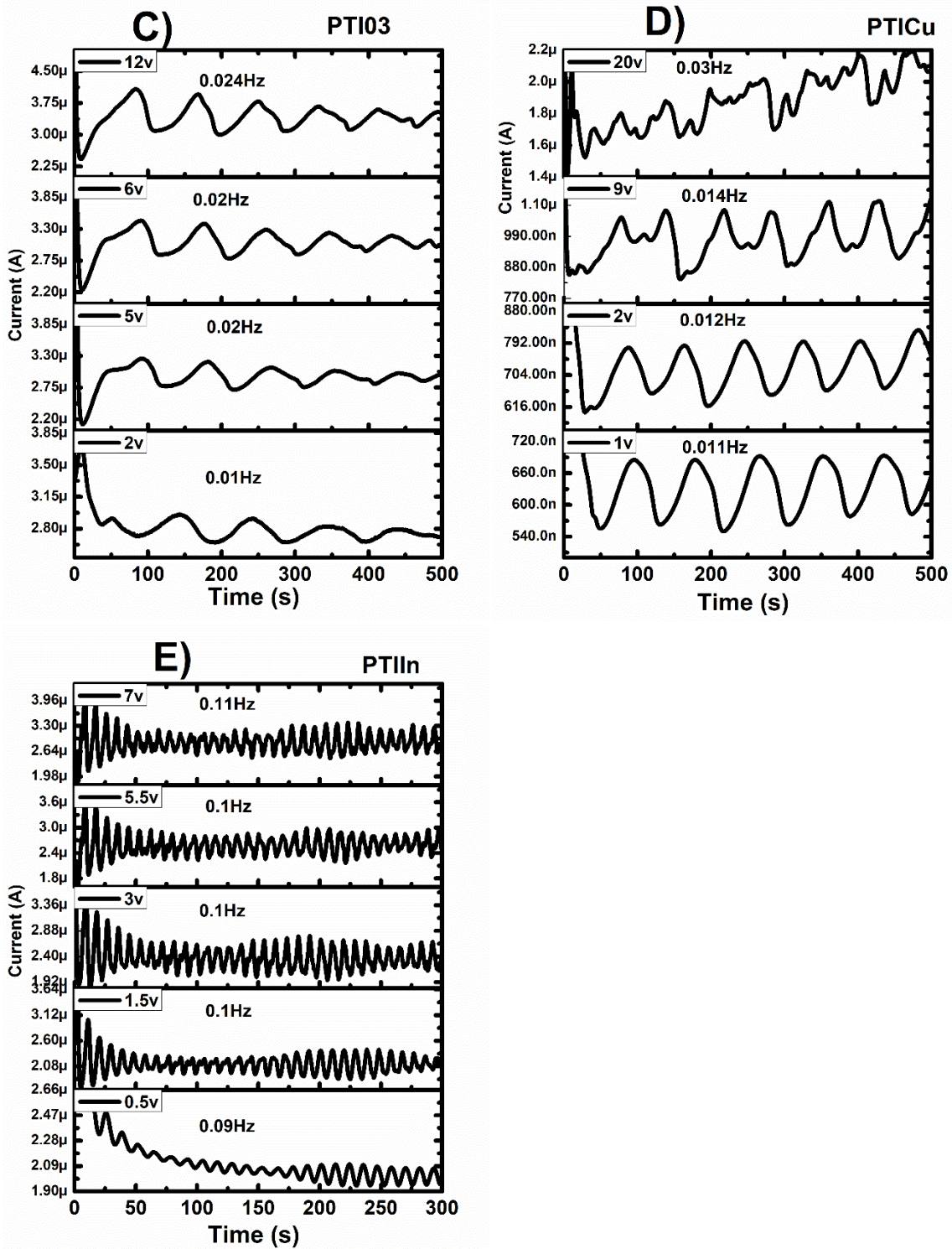


Figure 17. Current-time curves with different voltages a) PTIO1 b) PTIO2 c) PTIO3 d) PTICu e) PTIIn.

These oscillations are not defined by any additional external agent such as light or temperature. The measurements shown before were carried out under dark conditions. To see if the tunneling effect to produce oscillations is not thermal-assisted, the samples were tested at a lower temperature (than ambient) by using a Peltier cell. Figure 18 shows the current-time curves obtained at low temperatures (reaching 0° C). It is clear that there are no oscillations like the ones shown in figure 17. One could think that oscillations are then temperature-dependent, and that the threshold temperature is not reached at 0 °C; however, one should expect even lower currents. Then, the most plausible explanation of this result is that the humidity of the ambient could condense on the sample, producing direct conducting paths. This is why the current is orders of magnitude higher. It is not possible to conclude something about the oscillations vs temperature. Moreover, the magnitude of the oscillations at room temperature is around micro amperes, which could not be attributed to thermal effect a room temperature. It would mean that room temperature contains enough energy to excite the oscillators even that these oscillators do not need a primary excitation source (voltage), and in this work it is observed that there is a minimum voltage to the oscillator works.

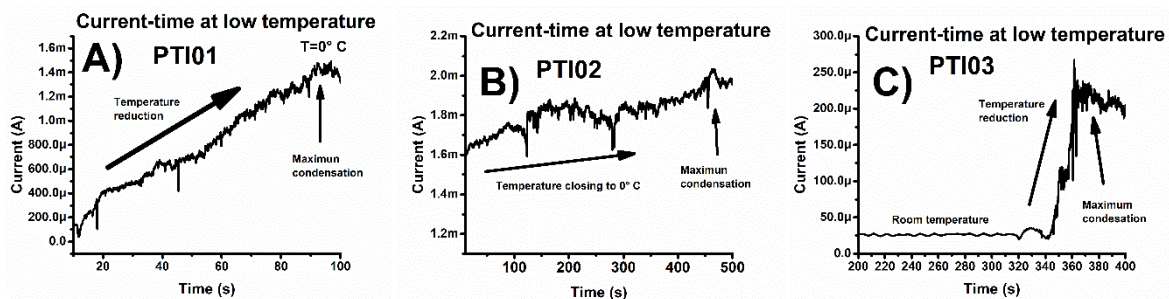


Figure 18. Current-time at low temperatures a) PTI01 b) PTI02 c) PTI03.

Also, I-V curves obtained at different voltage sweep rates were carried out to find any dependency of the oscillations on this parameter. In figure 19, curves obtained at three velocities can be observed. In all samples, the NDR effect is present, and the oscillations show an apparent tendency: as the sweep velocity increases, the frequency of oscillations decreases. At higher sweep rates, the heterostructures, that have a characteristic relaxation time, may be unable to follow the voltage changes, limiting the oscillation frequency. However, a baseline current increases, probably because it is displacement current. The displacement current (i_d) directly depends on the voltage change in time: $i_d = C \, dV/dt$, where C is the capacitance of the device, and dV/dt is the voltage sweep rate in the present case.

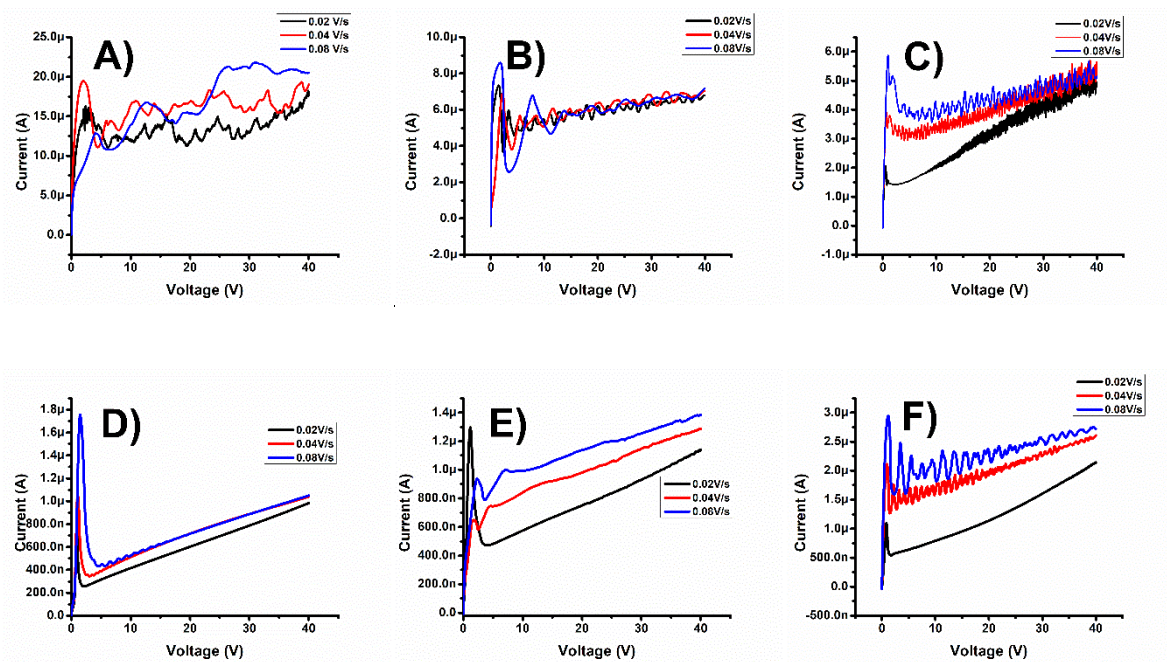


Figure 19. Current-voltages curves at different voltage sweep rates for samples a) PTI01 b) PTI02 c) PTI03 d) PTI04 e) PTICu f) PTII

As additional information, it is important to know the transport mechanisms in the heterostructures, since the conductivity is ruled by different parameters. In Figure 20 shows

the I-V curves in the log-log plot together with fitting of one transport mechanism “space charge limited current” (SCLC), the analysis of the transport mechanism presents different regions as can be seen in Figures from 11a to 11g. In low voltages, the behavior is linear (first region), the NDR effect is presented in the second region, and the periodic oscillations are displayed in the third region. In this case, the first region fits for the SCLC transport mechanism. Meanwhile, the second and third regions could be a result of charge and discharge through the whole structure because of the heterostructure, as we mentioned.

All graphs in Figure 20 display the SCLC mechanism in the first region (before the decreasing of the current). These graphs show that the current follows a power-law dependence. This behavior is characteristic of the SCLC mechanism [50, 75]. As is claimed by Tzolov et al. [75], this kind of behavior appears if the transient time of the charge carriers is smaller than the dielectric relaxation time. According to Tzolov et al. [75], this kind of transport is not related to the metal contact or the heterostructure but the bulk of the contacting materials. The bulk and the junction regions are connected in series, and the current is determined by the rate-limiting mechanism [75]. However, Marin et al. [50] claim that the SCLC has been associated to a negligible density of free carriers compared to carriers injected from the contacts, which added to the high decrease of conductivity indicate that, effectively, the crystalline silicon structures are carrier depleted. The SCLC transport mechanism is given for the next expression

$$I = aV + bV^n \quad [76] \quad (eq. 8)$$

The first term of the expression can be omitted. Thus the expression is reduced to

$$I = bV^n \quad [76] \quad (eq. 9)$$

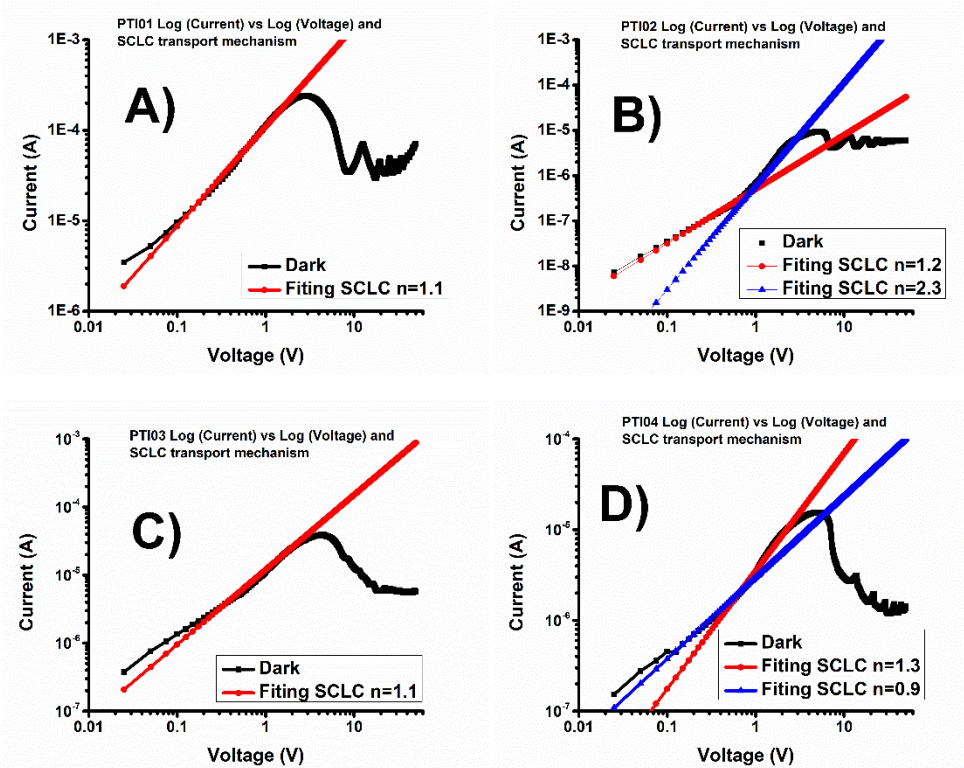
As can be noticed in the graphs from Figure 20, the SCLC mechanism is presented in all samples with different “n” values. This “n” value is related to the distribution of localized states [76]. When “n” takes a value close to 1 is the result of free-carrier conduction. Otherwise, n=2 corresponds to the SCLC region where all trap levels are occupied, and n>2 refers to the SCLC in trap filling region [77]. Other possibilities about n>2 is the following. The first one on account of the uniform distribution of space charge between electrodes [76] or the second one owing to surface states [78]. The n<1 can be a result of a different transport mechanism, for that reason in Figure 20h is presented a plot $\text{Ln}(J/V^2)$ vs $(1/V)$, where it shows two conduction regions similar to reported in the reference [79]. The first region shows a logarithmic behavior, which indicates a direct tunneling regime (this is an important point to take into account because in the next section, this regime will be very important to explain some effects) [79]. The second region shows a linear behavior, which could indicate Fowler-Nordheim tunneling or field-effect conduction mechanism [79]. In equations 10 and 11 are presented the mathematical description for each region. We believe that in low voltages before the NDR effect, the SCLC mechanism is presented since there is any modification of the curve and keeps its evolution in current before the NDR effect is presented. On the other hand, in high voltages, a Fowler-Nordheim tunneling (for n>2) and charge-discharge (for the oscillations) effect is observed, and as the own effect mention there is a tunneling effect in the heterostructure producing the NDR effect and the TiO₂ produces the capacitance that generates the charge-discharge effect after the maximum current peak observed in I-V curves that can clearly observed in figure 20.

$$\text{Ln}(j/V^2) \propto \text{Ln}\left(\frac{1}{V}\right) - (2d/\hbar)\sqrt{2m_e^*\phi} \quad [79] \text{ region I} \quad (\text{eq. 10}) \text{ and}$$

$$\ln(j/V^2) \propto (-4d\sqrt{2m^*}/3qh)\varphi^3(1/V) \quad [79] \text{ region II} \quad (\text{eq. 11})$$

Where d is the width silica, m_e^* is the electron effective mass, φ is the effective barrier height, and \hbar is the Planck constant.

Although we tried to cover all the possibilities for the transport mechanisms and the origin of the NDR effect, it is not possible to assure an absolute mechanism. However, these models are good approximations to explain these effects for these samples. Until now, no one has reported this effect and proposed a model that relates the NDR and the oscillations observed by us.



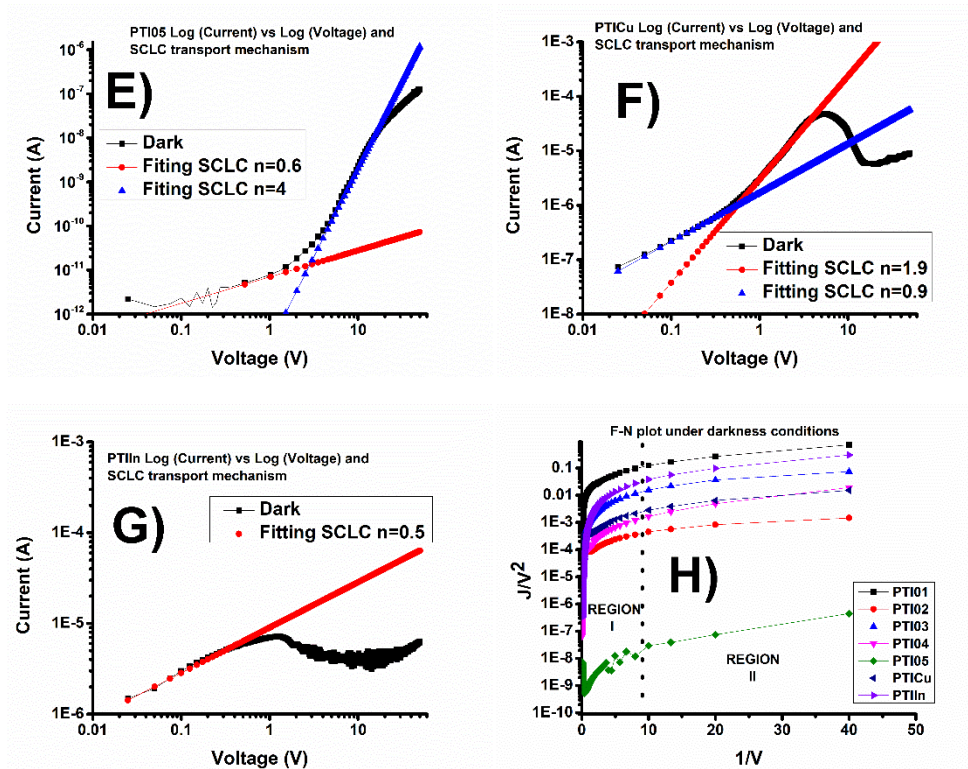


Figure 20. SCLC and Fowler-Nordheim transport mechanism analysis a) PTI01 b) PTI02 c) PTI03 d) PTI04 e) PTI05 f) PTICu g) PTIIn h) Fowler-Nordheim tunneling of all samples

3.5 Application as photosensor

Semiconductor heterojunctions are promising candidates for the fabrication of optoelectronic devices. As a major advantage, large bandgap semiconductors can be used as the top layer of the heterojunction where they serve as transparent window for the transmission of incoming light as well as charge collecting electrode. Despite the long history of all-inorganic counterparts, the hybrid organic-inorganic heterojunctions with the key property of low-temperature solution-based fabrication process have been considered just recently. Photodetector or light sensor are devices that detect electromagnetic radiation according to the detection are classified but basically work under illumination, the electric field at the

depletion region separates the photo-generated electron-hole pairs so that the excess holes are transmitted to the p-type semiconductor and the excess electrons are pushed toward the bulk of n-type where they are injected into the external circuit producing a current signal [80].

The I-V curves show a photocurrent effect in all samples as could be seen in Figure 12, but the samples PTI02, PTI04, and PTICu present the most pronounced effect. Table 3 shows the current values in dark and illumination conditions (the measurements in darkness were carried out inside of a dark metallic box, while the illumination conditions were carried out by using a white light lamp of 1000 lumens), and the current gain in certain voltage by mean the relation between photocurrent (I_{ph}) and dark current (I_{dark}). It means I_{ph}/I_{dark} . These values are taken from the I-V curves from Figure 12.

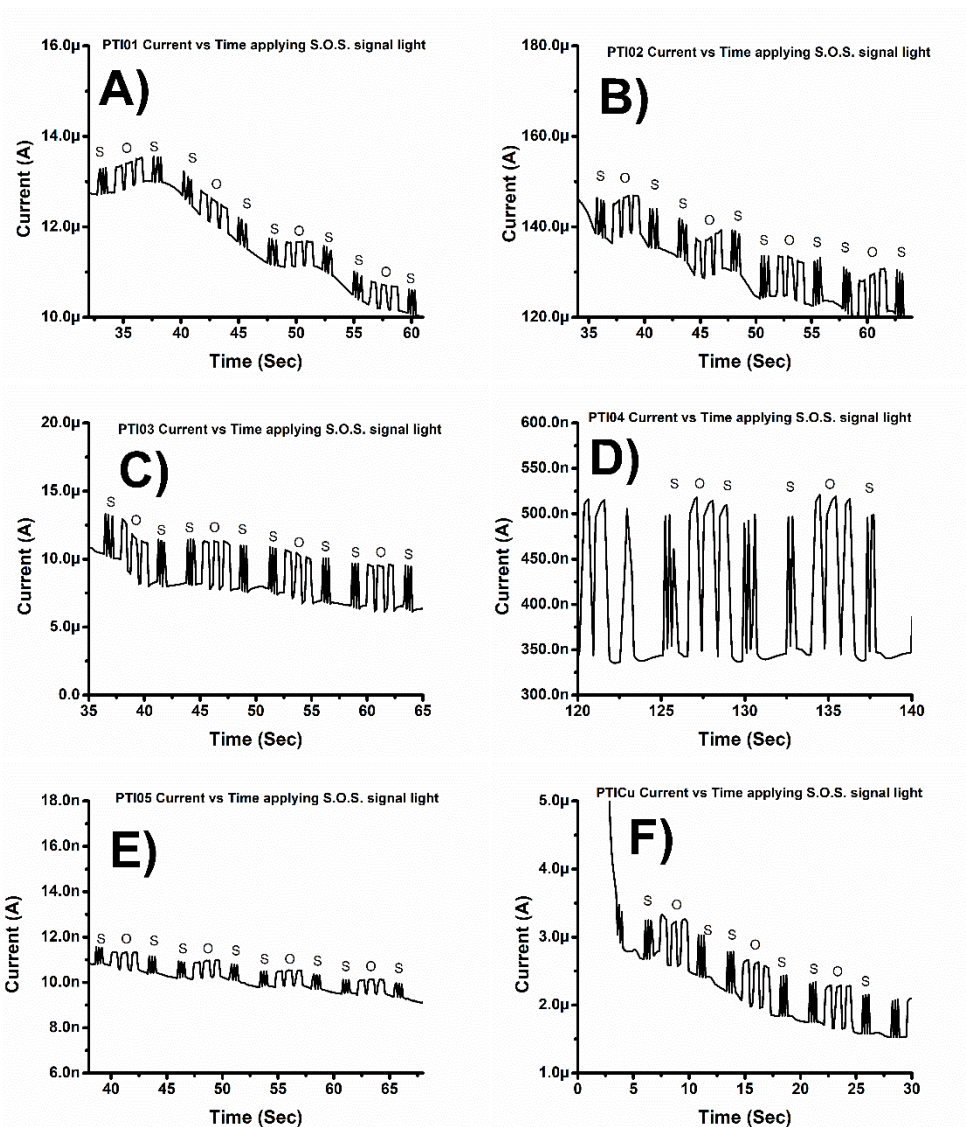
Table 3. Current gain of the sample at -5V and 18V

Sample	$I_{dark}(mA)$ at -5V	$I_{ph}(mA)$ at -5V	Current gain at - 5V	$I_{dark} (\mu A)$ at 18V	$I_{ph} (\mu A)$ at 18V	Current gain at 18V
PTI01	4.33	4.09	0.945	31.2	51.7	1.65
PTI02	0.202	0.423	2.088	6.61	8.34	1.34
PTI03	9.78	-9.99	1.021	3.76	7.81	2.076
PTI04	3.68	4.82	1.309	1.63	2.54	1.55
PTI05	8.36×10^{-6}	1.48×10^{-5}	1.77	0.0173	0.0108	0.624
PTICu	7.09	8.77	1.236	5.8	105	18.103
PTIIn	9.05	9.92	1.096	4.05	4.38	1.081

As could be seen in Figure 12 the samples displayed photocurrent effect. For that reason we performed I-t curves applying white light with the aim to observe the behavior. In Figure 21 can be observed the resulted, all the samples responded to the white light even we applied a S.O.S. signal and the samples following that controlled perturbation. As could be observed in Figure 14 the samples PTI04 and PTI05 does not presented the oscillation effect; however, these samples following the white light signal. The rest of the samples not only following the S.O.S. signal but also showed the natural oscillations, therefore, these samples displayed the white light pulses riding on the oscillations.

Also these heterostructures could be used as photodetector, thanks to the pulses. These pulse possess two edges, a rising and falling edge, which in the ideal case these values are zero. In an accurate digital signal, it is considered that the rise time starts when the pulse passes from 10 to 90% of its final amplitude for measurements purposes. The samples presented the following rising and falling times. PTI01 shows rising and falling for the “S” pulse 92.5 ms and 95.4 ms and for “O” pulse 104 ms and 96 ms. PTI02 displays rising and falling for the “S” pulse 97.5 ms and 92 ms and for “O” pulse 168 ms and 94.7 ms. PTI03 shows rising and falling for the “S” pulse 98 ms and 96.5 ms and for “O” pulse 101 ms and 106 ms. PTI04 get rising and falling for the “S” pulse 90 ms and 94 ms and for “O” pulse 95.4 ms and 232 ms. PTI05 presents rising and falling for the “S” pulse 98 ms and 102 ms and for “O” pulse 98 ms and 103 ms. PTICu get rising and falling for the “S” pulse 93.5 ms and 96.4 ms and for “O” pulse 98 ms and 108 ms. Finally the PTIIn shows rising and falling for the “S” pulse 94 ms and 94 ms and for “O” pulse 105.5 ms and 205 ms. The response on these heterostructures seems to be adequate to develop electronic devices. Other investigations report rising and falling times of 200 and 300 ms, respectively [81]. Even in a previous work reported by using organic semiconductors in the most of cases we are under the 100 ms, in average 95 ms,

which means the coating with TiO_2 generates a better response. The only inconvenient is the natural oscillation produced in the samples, but the PTI04 and PTI05 do not show this problem. Moreover, another advantage is the operation voltage since is very low 5 V and also could be biased with negative voltages and the response is identical. The obtaining of these heterostructures by a straightforward method give us heterostructures that could be used in some electronics application.



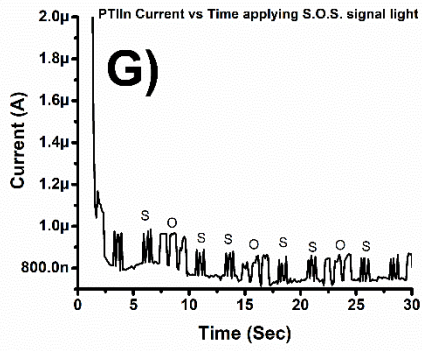


Figure 21. Current-time curves applying a S.O.S. signal light a) PTI01, b) PTI02, c) PTI03, d) PTI04, e) PTI05, f) PTICu, and g) PTIn.

References

- [1] Z. Huang, N. Geyer, P. Werner, J. de Boor, U. Gösele, Metal-Assisted chemical etching of silicon: a review, *Adv. Mater.* 23, 285 (2010). <https://doi.org/10.1002/adma.201001784>
- [2] E. Quiroga-González, M.Á. Juárez-Estrada, E. Gómez-Barojas, (Invited) light enhanced metal assisted chemical etching of silicon, *ECS Trans.* 86, 55 (2018). <https://doi.org/10.1149/08601.0055ecst>
- [3] D.H. Everett, IUPAC, manual of symbol and terminology for physico-chemical quantities and units, appendix, definitions, terminology and symbols in colloid and surface chemistry, Part I, *Pure Appl. Chem.* 31, 579 (1972). <http://dx.doi.org/10.1351/pac197231040577>
- [4] Shiping Xu, Xiang Sun, Yuan Gao, Min Yue, Qinyan Yue, Baoyu Gao, Solvent effects on microstructures and properties of three-dimensional hierarchical TiO₂ microsphere structures synthesized via solvothermal approach, *J. Solid State Chem.* 253, 167 (2017). <https://doi.org/10.1016/j.jssc.2017.05.001>
- [5] S. Sampath, P. Maydannik, T. Ivanova, M. Shestakova, T. Homola, A. Bryukvin, M. Sillanpää, R. Nagumothu, V. Alagan, Efficient solar photocatalytic activity of TiO₂ coated nano-porous silicon by atomic layer deposition *Superlattices Microstruct.* 97, 155 (2016). <https://doi.org/10.1016/j.spmi.2016.06.004>
- [6] Y. Wang, Y.R. Su, L. Qiao, L.X. Liu, Q. Su, C.Q. Zhu, X.Q. Liu, Synthesis of one-dimensional TiO₂/V₂O₅ branched heterostructures and their visible light photocatalytic activity towards Rhodamine B, *Nanotechnology* 22, 225702 (2011). <https://doi.org/10.1088/0957-4484/22/22/225702>
- [7] Y. Tonga, Q. Huang, S. Ana, Q. Rena, L. Zhanga, Y. Dinga, X. Lub, Y. Zhaoa, X. Zhanga, Photonic enhanced thin-film solar cells with conformal nanostructure, *Sol. Energy* 173, 504 (2018). <https://doi.org/10.1016/j.solener.2018.04.007>
- [8] W.-J. Lee, Y.-H. Choa, Highly conformal carbon-doped SiCN films by plasma-enhanced chemical vapor deposition with enhanced barrier properties, *Thin Solid Films* 657, 32 (2018). <https://doi.org/10.1016/j.tsf.2018.04.042>

- [9] A. Augustin, K. Rajendra Udupa, K. Udaya Bhat, Effect of coating current density on the wettability of electrodeposited copper thin film on aluminum substrate, *Perspect. Sci.* 8, 472 (2016). <https://doi.org/10.1016/j.pisc.2016.06.003>
- [10] R. Fernández-Acosta, E. Peláez-Abellán, J.R. Correa, U. Jáuregui-Haza, Nanostructured TiO₂ obtained by electrolysis and its application in the remediation of water polluted with paracetamol, *Int. J. Chem. Mater. Environ. Res.* 3, 20 (2016).
- [11] K.-R. Zhu, M.-S. Zhang, J.-M. Hong, Z. Yin, Size effect on phase transition sequence of TiO₂ nanocrystal, *Mater. Sci. Eng. A* 403, 87 (2005). <https://doi.org/10.1016/j.msea.2005.04.029>
- [12] Biswajit Choudhury, Munmun Dey, Amarjyoti Choudhury, Defect generation, d-d transition, and band gap reduction in Cu-doped TiO₂ nanoparticles, *Int. Nano Lett.* 3, 25 (2013). <https://doi.org/10.1186/2228-5326-3-25>
- [13] Z. Lan, Y. Yu, S. Yan, E. Wang, J. Yao, Y. Cao, Synergetic effect of N³⁻, in³⁺ and Sn⁴⁺ ions in TiO₂ towards efficient visible photocatalysis, *J. Photochem. Photobiol. A Chem.* 356, 132 (2018). <https://doi.org/10.1016/j.jphotochem.2017.12.032>
- [14] Muhammad Tahir, Nor Aishah Saidina Amin, Indium-doped TiO₂ nanoparticles for photocatalytic CO₂ reduction with H₂O vapors to CH₄, *Appl. Catal. B Environ.* 162, 98 (2015). <https://doi.org/10.1016/j.apcatb.2014.06.037>
- [15] S.M. Mokhtar, M.K. Ahmad, C.F. Soon, N. Nafarizal, A.B. Faridah, A.B. Suriani, M.H. Mamat, M. Shimomura, K. Murakami, Fabrication and characterization of rutile-phased titanium dioxide (TiO₂) nanorods array with various reaction times using one step hydrothermal method, *Optik* 154, 510 (2018). <https://doi.org/10.1016/j.ijleo.2017.10.091>
- [16] Priyanka Dwivedia, Neha Chauhanb, P. Vivekanandanb, Samaresh Dasa, D. Sakthi Kumarb, Saakshi Dhanekara, Scalable fabrication of prototype sensor for selective and sub ppm level ethanol sensing based on TiO₂ nanotubes decorated porous silicon, *Sens. Actuators B* 249, 602 (2017). <https://doi.org/10.1016/j.snb.2017.03.154>
- [17] W.F. Zhang, Y.L. He, M.S. Zhang, Z. Yin, Q. Chen, Raman scattering study on anatase TiO₂ nanocrystals, *J. Phys. D* 33, 912 (2000). <https://doi.org/10.1088/0022-3727/33/8/305>
- [18] Patricia M. Perillo, Daniel F. Rodriguez, Growth control of TiO₂ nanotubes in different physical environments, *Nanosci. Methods* 1, 194 (2012). <https://doi.org/10.1080/17458080.2012.663507>

- [19] M.K. Ahmad, S.M. Mokhtar, C.F. Soon, N. Nafarizal, A.B. Suriani, A. Mohamed, M.H. Mamat, M.F. Malek, M. Shimomura, K. Murakami, Raman investigation of rutile-phased TiO₂ nanorods/nanoflowers with various reaction times using one step hydrothermal method, *J. Mater. Sci.* 27, 7920 (2016). <https://doi.org/10.1007/s10854-016-4783-z>
- [20] M. Najafi, A. Kermanpur, M.R. Rahimpour, A. Najafizadeh, Effect of TiO₂ morphology on structure of TiO₂-graphene oxide nanocomposite synthesized via a one-step hydrothermal method, *J. Alloy. Compd.* 722, 272 (2017). <https://doi.org/10.1016/j.jallcom.2017.06.001>
- [21] M. Lubas, J.J. Jasinski, M. Sitarz, L. Kurpaska, P. Podsiad, J. Jasinski, Raman Spectroscopy of TiO₂ thin films formed by hybrid treatment for biomedical applications, *Spectrochim. Acta A Mol. Biomol. Spectrosc.* 133, 867 (2014). <https://doi.org/10.1016/j.saa.2014.05.045>
- [22] K. Zakrzewska, Nonstoichiometry in TiO_{2-y} Studied by Ion Beam Methods and Photoelectron Spectroscopy, *Adv. Sci. Eng. Mater.* 2012, 1-14 (2011). <https://doi.org/10.1155/2012/826873>
- [23] X. Xue, W. Ji, Z. Mao, H. Mao, Y. Wang, X. Wang, W. Ruan, B. Zhao, J.R. Lombardi, Raman investigation of nanosized TiO₂: effect of crystallite size and phonon confinement, *J. Phys. Chem. C* 116, 8792 (2012). <https://doi.org/10.1021/jp2122196>
- [24] F.S. Al mashary, S. de Castro, A.F. da Silva, J.F. Felix, M.R. Piton, Helder. Viní. Avança Galeti, A. De Giovanni Rodrigues, Yara. Galvão. Gobato, N. Al Saqri, M. Henini, M.M. Al huwayz, A.M. Albadri, A.Y. Alyamani, H.A. Albrathen, S.A. Alhusaini, K.M. Aljaber, A.Z. Alanazi, F.S. Alghamdi, Effect of growth techniques on the structural, optical and electrical properties of indium doped TiO₂ thin films, *J. Alloy. Compd.* 766, 194 (2018). <https://doi.org/10.1016/j.jallcom.2018.06.360>
- [25] I. Leontis, A. Othonos, A.G. Nassiopoulou, Structure, morphology, and photoluminescence of porous Si nanowires: effect of different chemical treatments *Nanoscale Res. Lett.* 8, 383 (2013). <https://doi.org/10.1186/1556-276X-8-383>
- [26] Canham, Leigh & Knovel (Firm), Properties of porous silicon, London, 1997
- [27] Nassiopoulou A. G, Encyclopedia of Nanoscience and Nanotechnology, Silicon nanocrystals and nanowires embedded in SiO₂, ed. By Nalwa H. S. (California: American Scientific Publishers, 2004)

- [28] H. Mizuno, H. Koyama, N. Koshida, Oxide-free blue photoluminescence from photochemically etched porous silicon, *Appl. Phys. Lett.* 8, 3779 (1996). <https://doi.org/10.1063/1.116996>
- [29] M.V. Wolkin, J. Jorne, P.M. Fauchet, G. Allan, C. Delerue, Electronic states and luminescence in porous silicon quantum dots: the role of oxygen, *Phys. Rev. Lett.* 82, 197 (1999). <https://doi.org/10.1103/PhysRevLett.82.197>
- [30] E. Lioudakis, A. Othonos, A.G. Nassiopoulou, Ultrafast transient photoinduced absorption in silicon nanocrystals: Coupling of oxygen-related states to quantized sublevels, *Appl. Phys. Lett.* 8, 171103 (2007). <https://doi.org/10.1063/1.2728756>
- [31] L.T. Cong, N.T. Ngoc Lam, N.T. Giang, P.T. Kien, N.D. Dung, N.N. Ha, N-type silicon nanowires prepared by silver metal-assisted chemical etching: Fabrication and optical properties, *Mater. Sci. Semicond. Process.* 90, 198 (2019). <https://doi.org/10.1016/j.mssp.2018.10.026>
- [32] G.D. Sanders, Y.C. Chang, Theory of optical properties of quantum wires in porous silicon, *Phys. Rev. B* 45, 9202 (1992). <https://doi.org/10.1103/PhysRevB.45.9202>
- [33] K.W. Cheah, T. Chan, W.L. Lee, D. Teng, W.H. Zheng, Q.M. Wang, Multiple peak photoluminescence of porous silicon, *Appl. Phys. Lett.* 63, 3464 (1993). <https://doi.org/10.1063/1.110121>
- [34] F. Labreche, A. Berbadj, N. Brihi, R. Karima, B. Jamoussi, Green photoluminescence, structural and optical properties of Nd-TiO₂ thin films *Optik* 172, 63 (2018). <https://doi.org/10.1016/j.ijleo.2018.06.131>
- [35] T.T. Loan, V.H. Huong, V.T. Tham, N.N. Long, Effect of zinc doping on the bandgap and photoluminescence of Zn²⁺-doped TiO₂ nanowires, *Phys. B* 532, 210 (2018). <https://doi.org/10.1016/j.physb.2017.05.027>
- [36] G. Santamaría-Juárez, E. Gómez-Barojas, E. Quiroga-González, E. Sánchez-Mora, J.A. Luna-López, Oxidized porous silicon as a non-interfering support for luminescent dyes, *Mesoporous Biomater* 3, 61 (2016). <https://doi.org/10.1515/mesbi-2016-0008>
- [37] Barun Sarkar Mitra, Aniruddha Mondal, Bijit Choudhuri, Bikram Kishore Mahajan, Shubhro Chakrabartty, Chitralkh Nangbam, Enlarged broad band photodetection using Indium doped TiO₂ alloy thin film, *J. Alloy. Comp.* 615, 440 (2014). <https://doi.org/10.1016/j.jallcom.2014.06.184>

- [38] N.A. Al Saqri, A. Mondal, J.F. Felix, Y.G. Gobato, V.O. Gordo, H. Albalawi, D. Jameel, H. Alghamdi, F. Al Mashary, D. Taylor, M.S. Abd El-sadek, M. Henini, Investigation of defects in indium doped TiO₂ thin films using electrical and optical techniques, *J. Alloy. Comp.* 698, 883 (2017). <https://doi.org/10.1016/j.jallcom.2016.12.294>
- [39] S. Mathew, P. Ganguly, S. Rhatigan, V. Kumaravel, C. Byrne, S. Hinder Hinder, J. Bartlett, M. Nolan, S. Pillai, Cu doped TiO₂: visible light assisted photocatalytic antimicrobial activity and high temperature anatase stability. *Appl. Sci.* 8 2067 (2018). <https://doi.org/10.3390/app8112067>
- [40] A. Kux, M. Ben Chorin, Band Gap of porous silicon, *Phys. Rev. B* 51, 17535 (1995). <https://doi.org/10.1103/PhysRevB.51.17535>
- [41] Mosad, A. G., Fouda, M. E., Khatib, M. A., Salama, K. N., & Radwan, A. G. Improved memristor-based relaxation oscillator. *Microelectronics Journal*, 44, 814 (2013). <https://doi.org/10.1016/j.mejo.2013.04.005>
- [42] Elwakil, A. S., & Kennedy, M. P. (2000). A low-voltage, low-power, chaotic oscillator, derived from a relaxation oscillator. *Microelectronics Journal*, 31, 459 (2000). [https://doi.org/10.1016/S0026-2692\(99\)00150-0](https://doi.org/10.1016/S0026-2692(99)00150-0)
- [43] P. Ramesh, C. Suresh Kumar, Studies on gold/porous silicon/crystalline silicon junctions, *J. Porous Mater.* 7, 299 (2000). <https://doi.org/10.1023/A:1009604703115>
- [44] A. Garzon-Roman, C. Zuniga-Islas, E. Quiroga-Gonzalez, Modulation of morphology and optical characteristics of TiO₂ grown into porous silicon by an easy approach, *J. Mater. Sci. Mater. Electron.* 30, 21503 (2019). <https://doi.org/10.1007/s10854-019-02540-1>
- [45] A. Mortezaali, S. Ramezani Sani, F. Javani Jooni, Correlation between porosity of porous silicon and optoelectronic properties, *J. Non-Oxide Glasses* 1, 293 (2009).
- [46] J.T. Frederiksen, P.G. Melcher, E. Veje, Electrical band-gap energy of porous silicon and the band offsets at the porous-silicon/crystalline-silicon heterojunction measured versus sample temperature, *Phys. Rev. B* 58, 8020 (1998). <https://doi.org/10.1103/PhysRevB.58.8020>
- [47] V. M. Aroutiounian, M. Zh. Ghulinyan Electrical conductivity mechanisms in porous silicon *phys. stat. sol. (a)* 197, 462 (2003). <https://doi.org/10.1002/pssa.200306545>

- [48] Rolfe C. Anderson, Richard S. Muller, and Charles W. Tobias Investigations of the Electrical Properties of Porous Silicon *J. Electrochem. Soc.* 138, 3406 (1991). <https://doi.org/10.1149/1.2085423>
- [49] L Esaki, New Phenomenon in Narrow Germanium p – n Junctions, *Phys. Rev.* 109, 603 (1958). <https://doi.org/10.1103/PhysRev.109.603>
- [50] Marin O, Toranzos V, Urteaga R, Comedi D, and Koropeccki RR, Negative differential resistance in porous silicon devices at room temperature. *Superlattice and Microst.* 79, 45 (2015). <https://doi.org/10.1016/j.spmi.2014.12.019>
- [51] J Hu, W Xiong, P Huang, Y Wang, C Cai, J Wang 2020 First-principles study on strain modulated negative differential resistance effect of in-plane device based on heterostructure tellurene. *Appl. surf. sci.* 528, 146957 (2020). <https://doi.org/10.1016/j.apsusc.2020.146957>
- [52] JJ Guttman, CB Chambers, AR Villagracia, GN Santos, PR Berger, Negative differential resistance in polymer tunnel diodes using atomic layer deposited, TiO₂ tunneling barriers at various deposition temperatures, *Org. Electron.* 47, 228 (2017). <https://doi.org/10.1016/j.orgel.2017.05.015>
- [53] F Ning, SZ Chen, Y Zhang, GH Liao, PY Tang, ZL Li, LM Tang, Interfacial charge transfers and interactions drive rectifying and negative differential resistance behaviors in InAs/graphene van der Waals heterostructure. *Appl. Surf. Sci.* 496, 143629 (2019). <https://doi.org/10.1016/j.apsusc.2019.143629>
- [54] WH Xiao, F Xie, XJ Zhang, YF Chu, JP Liu, HY Wang, ZQ Fan, MQ Long, KQ Chen, Large negative differential resistance behavior in arsenene nanoribbons induced by vacant defects, *Phys. Lett. A* 383 1629 (2019). <https://doi.org/10.1016/j.physleta.2019.02.022>
- [55] Z Yu, M Aceves, F Wang, J Carrillo, R Kiebach, K Monfil 2008 Room temperature quantum tunneling and Coulomb blockade in silicon-rich oxide. *Physica E: Low-dimens. Syst. Nanostruct.* 41 264 (2008). <https://doi.org/10.1016/j.physe.2008.07.022>
- [56] J Zhang, Z Qin, B Xu, G Song, Low bias negative differential resistance with dual peaks based on octacene molecular device. *Phys. Lett. A* 383 2948 (2019). <https://doi.org/10.1016/j.physleta.2019.06.044>
- [57] I Najeh, L El Mir, The effects of the applied current and the measurement temperature on the negative differential resistance behaviour of carbonized xerogel. *Chem. Phys.* 524, 85 (2019). <https://doi.org/10.1016/j.chemphys.2019.04.032>

- [58] Nam Do, V, and Dollfus, P, Negative differential resistance in zigzag-edge graphene nanoribbon junctions, *J. Appl. Phys.* 107 063705 (2010). <https://doi.org/10.1063/1.3340834>
- [59] K Miyaji, T Hiramoto, Silicon Single Electron Transistors Operating at Room Temperature and Their Applications. *Comprehensive Semiconductor Science and Technology* 5, 340 (2011). 10.1126/science.275.5300.649
- [60] Y Du, H Pan, S Wang, T Wu, YP Feng, J Pan, A Thye, S Wee, Symmetrical Negative Differential Resistance Behavior of a Resistive Switching Device, *ACS Nano* 6, 2517 (2012). <https://doi.org/10.1021/nm204907t>
- [61] J Zeng, KQ Chen, J He, XJ Zhang, CQ Sun, Edge Hydrogenation-Induced Spin Filtering and Rectifying Behaviors in the Graphene Nanoribbon Heterojunctions. *J. Phys. Chem. C* 115, 25072 (2011). <https://doi.org/10.1021/jp208248v>
- [62] P Moffatt and EH Kim, Negative differential resistance from a van Hove singularity in tunnel diodes *Appl. Phys. Lett.* 89 192117 (2006). <https://doi.org/10.1063/1.2387119>
- [63] S. Zhao, Y. Chen, Z. Zhao, L. Jiang, C. Zhang, J. Kong, X. Zhu, Enhanced capacitance of TiO₂ nanotubes topped with nanograss by H₃PO₄ soaking and hydrogenation doping *Electrochim. Acta* 266, 233 (2018). <https://doi.org/10.1016/j.electacta.2018.02.037>
- [64] Nayfeh MH, Rao S, Nayfeh OM, Smith A, Therrien J, UV photodetectors with thin-film Si nanoparticle active medium, *IEEE Trans Nanotechnol.* 4 660 (2005). 10.1109/TNANO.2005.858606
- [65] J.M. Ginoux, C. Letellier, Van der Pol and the history of relaxation oscillations: toward the emergence of a concept, *Chaos, An Interdiscipl. J. Nonlin. Sci.* 22, 23120 (2012). <https://doi.org/10.1063/1.3670008>
- [66] J. Nagumo, M. Shimura, Self-oscillation in a transmission line with a tunnel diode, *Proc. IRE* 49, 1281 (1961). 10.1109/JRPROC.1961.287920
- [67] N Janene, N Ghrairi, A Allagui, H Alawadhi, MA El Khakani, B Bessais, M Gaidi, Opto-electronic properties of a TiO₂/PS/mc-Si heterojunction based solar cell. *Appl. Surf. Sci.* 368, 140 (2016). <https://doi.org/10.1016/j.apsusc.2016.01.231>
- [68] A Garzon-Roman, O Milosevic, ME Rabanal, Morphological, structural, and functional properties of vertically aligned carbon nanotubes deposited on porous silicon layers by ultrasonic spray pyrolysis, *Micropor. Mesopor. Mat.* 292 109738 (2020). <https://doi.org/10.1016/j.micromeso.2019.109738>

- [69] MO Erdal, A Kocyigit, M Yıldırım, The C-V characteristics of TiO₂/p-Si/Ag, GNR doped TiO₂/p-Si/Ag and MWCNT doped TiO₂/p-Si/Ag heterojunction devices. *Chin. J. Phys.* 64 163 (2020). <https://doi.org/10.1016/j.cjph.2019.12.021>
- [70] WA Farooq, M Atif, A Fatehmulla, IS Yahia, MS AlSalhi, M Fakhar-e-Alam, SM Ali, K Ali, T Munir, MA Manthrammel, Photovoltaic and capacitance measurements of solar cells comprise of Al-doped CdS (QD) and hierarchical flower-like TiO₂ nanostructured electrode, *Results in Physics* 16 102827 (2020). <https://doi.org/10.1016/j.rinp.2019.102827>
- [71] M Yıldırım, Characterization of the framework of Cu doped TiO₂ layers: An insight into optical, electrical and photodiode parameters. *J. Alloy. Compd.* 773 890 (2019). <https://doi.org/10.1016/j.jallcom.2018.09.276>
- [72] MO Erdal, A Kocyigit, M Yıldırım, The rate of Cu doped TiO₂ interlayer effects on the electrical characteristics of Al/Cu:TiO₂/n-Si (MOS) capacitors depend on frequency and voltaje. *Microelectron. Reliab.* 106 113591 (2020). <https://doi.org/10.1016/j.microrel.2020.113591>
- [73] Biswajit Das, Observation of capacitance–voltage oscillations in porous silicon. *Physica E* 23, 141 (2004). <https://doi.org/10.1016/j.physe.2004.01.016>
- [74] D. Bozyigit, W.M.M. Lin, N. Yazdani, O. Yarema, V. Wood, A quantitative model for charge carrier transport, trapping and recombination in nanocrystal-based solar cells, *Nat. Commun.* 6 6180 (2015). <https://doi.org/10.1038/ncomms7180>
- [75] M Tzolov, B Chang, A Yin, D Straus, and JM Xu, Electronic Transport in a Controllably Grown Carbon Nanotube-Silicon Heterojunction Array. *Phys. Rev. Lett.* 92 075505 (2005). <https://doi.org/10.1103/PhysRevLett.92.075505>
- [76] TA Burr, AA Seraphin, E Werwa, KD Kolenbrander, Carrier transport in thin films of silicon nanoparticles. *Phys. Rev. B* 56 4818 (1997). <https://doi.org/10.1103/PhysRevB.56.4818>
- [77] N Wan, LT Sun, SN Ding, T Xu, J Sun, HC Bi, Synthesis of graphene–CNT hybrids via joule heating: Structural characterization and electrical transport, *Carbon* 53 260 (2013). <https://doi.org/10.1016/j.carbon.2012.10.057>
- [78] JH Choi, SN Das, KJ Moon, JP Kar, JM Myoung, Fabrication and characterization of p-Si nanowires/ZnO film heterojunction diode. *Solid. Electron.* 54, 1582 (2010). <https://doi.org/10.1016/j.sse.2010.07.015>

- [79] Gallach-Pérez D, Muñoz-Noval A, García-Pelayo L, Manso-Silván M, and Torres-Costa V, Tunnel conduction regimes, white-light emission and band diagram of porous silicon–zinc oxide nanocomposites. *J. Lumin.* 191 107 (2017). <https://doi.org/10.1016/j.jlumin.2016.10.037>
- [80] Noroozi, A., Mosaddegh, A., & Abdi, Y. (2021). High-sensitivity and broadband PEDOT:PSS–silicon heterojunction photodetector. *Materials Science and Engineering: B*, 271, 115260 (2021). <https://doi.org/10.1016/j.mseb.2021.115260>
- [81] Q. Zafar, N. Fatima, K. S. Karimov, M. M. Ahmed, and K. Sulaiman, Realizing broad bandwidth visible wavelength photodiode based on solution-processed ZnPc/PC71BM diad. *Opt Mater.* 64, 131 (2017). <https://doi.org/10.1016/j.optmat.2016.12.001>

CHAPTER 4

CONCLUSION

This work has demonstrated the creation of heterostructures of PS decorated with TiO₂ by using simple and cost-effective synthetic methods, and that they present non-conventional effects. The morphology of the TiO₂ nanoparticles decorating the pore walls can be varied not only with the solvent but also with the titanium butoxide concentration. As the precursor concentration reduces, the morphology of the TiO₂ structure changes from 2D structures (nanosheets) to 0D structures (nanoparticles). Also, the variation of the solvent affects the morphology and the size of the TiO₂ structures; one can go from irregular nanoparticles (using ethylene glycol) to sea urchin structures (using acetone). Moreover, under certain conditions, a conformal deposition is obtained (using methanol). A combination of TiO₂ phases is obtained in the most of the cases, anatase the predominant phase. There is a clear dependency of the bandgap of TiO₂ with the structure, size and morphology of the samples. This has a clear implication in the energy of the photoluminescence of the samples.

The TiO₂/PS heterostructure conducts electricity when forward biased, like a normal rectifying diode. However, it presents oscillations when reversed biased. The behavior of the heterostructures at low reversed voltages is like a tunnel diode. A negative differential resistance (NDR) can be observed. Oscillations occur by a competition of minority and majority currents at the voltages of tunneling, which charge/discharge an intergrowth capacitor formed in the device. The oscillations are periodic, with a characteristic frequency. As they are explained by effects of charge and discharge of a capacitor connected in parallel with a diode (in the tunneling mode), the heterostructure is considered a relaxation oscillator

(the simplest ever reported). The oscillations can be modulated by varying the applied voltage or the voltage sweep rate. Additionally, this heterostructure with all its electronic transport characteristics, could also be used as photodetector with enhanced sensitivity due to the oscillations.

Products of this work

Abel Garzon Roman, C. Zúñiga-Islas, Enrique Quiroga-González Immobilization of doped TiO₂ nanostructures with Cu or In inside of macroporous silicon using the solvothermal method: Morphological, structural, optical and functional properties. September 2019. Ceramics International, volume 46, pages 1137-1147. DOI: 10.1016/j.ceramint.2019.09.082

Abel Garzon Roman, C. Zúñiga-Islas, Enrique Quiroga-González Modulation of morphology and optical characteristics of TiO₂ grown into porous silicon by an easy approach. November 2019. Journal of Materials Science: Materials in Electronics, volume 30, pages 21503-21513. DOI: 10.1007/s10854-019-02540-1

Abel Garzon Roman, Enrique Quiroga-González, C. Zúñiga-Islas Heterostructure of TiO₂ and macroporous silicon: The simplest relaxation oscillator. January 2021. Journal of Science: Advanced Materials and Devices, volume 6, pages 209-214.

Patent request: OSCILADOR DE RELAJACIÓN A PARTIR DE DIÓXIDO DE TITANIO Y SILICIO POROSO. Registration number: MX2021013506. Submitted on November 4th, 2021. Inventors: **Abel Garzon Roman (34%)**, Enrique Quiroga-González (33%), C. Zúñiga-Islas (33%).